Design of Replacement Structural Components for Fabrication using Metal Big Area Additive Manufacturing

A Thesis
Presented to
The Academic Faculty

by

Clayton Greer

In Partial Fulfillment
of the Requirements for the Degree
Master of Science in the
George W. Woodruff School of Mechanical Engineering

Georgia Institute of Technology
May 2017

**Design of Replacement Structural Components for Fabrication using Metal Big
Area Additive Manufacturing**

Approved by:

Dr. Thomas Kurfess Advisor
School of Mechanical Engineering
Georgia Institute of Technology

Dr. Christopher Saldana
School of Mechanical Engineering
Georgia Institute of Technology

Dr. Lonnie Love
Manufacturing Systems Research Group
Oak Ridge National Laboratory

Date Approved: March 31, 2017

To My Parents

ACKNOWLEDGEMENTS

TABLE OF CONTENTS

LIST OF TABLES

LIST OF FIGURES

SUMMARY

Since the 1980s, additive manufacturing processes, commonly called 3D printing, have been used for prototyping applications due to low part strength. A new wire-feed metal additive manufacturing process called Metal Big Area Additive Manufacturing (MBAAM) addresses the component strength and deposition rates for large structural components. MBAAM uses gas metal arc welding to deposit steel welding wire in 3D structures. The design protocols for designing structural components using MBAAM are presented in this thesis using a case study in designing and printing a replacement excavator arm. In additive manufacturing, deposition rate and feature resolution are inversely related, which affects the design strategy of additive manufacturing processes that use high deposition rates. For instance, MBAAM deposits steel beads that are 6mm. The excavator arm is designed to use plates with thicknesses intermediate between the thickness of one and two beads deposited with MBAAM, so topology optimization is used to reduce the weight of the arm design using thicker walls. Structures printed with MBAAM must be designed to adhere to an overhang constraint of 15° and minimize the use of support structures because the support structures are full strength steel. Removal of the solid supports requires CNC machining, which is expensive and time consuming. The overhang constraint requires the modification of features in the excavator arm, requiring geometry changes and post-processing machining to implement the needed features. The structural integrity of this modified arm is analyzed using finite element analysis to ensure that the arm will not fail in normal operation. The printed arm is subsequently installed on an excavator and used in a real world demonstration.

CHAPTER 1. INTRODUCTION

Additive manufacturing (AM) has recently garnered mainstream attention for production of final products. Early additive manufacturing techniques such as stereolithography and selective laser sintering were used for prototyping of functional models and tooling because they took less time to produce custom geometry than traditional methods, such as machining. Since then, progress in mechanical properties and materials selection has shifted the focus of additive manufacturing to end-use manufacturing of parts delivered directly to the customer, instead of the prototypes or molds that were used to design and fabricate the delivered part. However, currently available processes have low deposition rates and small build volumes. Recent steps to increase build rates and volumes have seen the development of a large scale fused deposition modeling system known as Big Area Additive Manufacturing (BAAM). BAAM deposits polymer matrix composites at rates in excess of 39,000 cm^3/hr, compared to desktop and industrial systems at 15-85 cm^3/hr. Polymer matrix composites, while strong and lightweight, are not suited to replace metals and alloys for scenarios such as high strength, high temperature, and high contact wear applications. A new system called Metal Big Area Additive Manufacturing (MBAAM), is a wire-fed arc weld deposition system that deposits standard steel weld filler wire in an open environment. Other wire feed metal AM processes use high cost laser and electron beam systems that require an inert environment. The available materials for MBAAM include all weldable materials such as steel, stainless steel, aluminum, titanium, and nickel alloys. The deposition rate is around 600 cm^3/hr; in contrast, powder bed fusion processes such as electron beam melting and selective laser melting have deposition rates nominally between 25-120 cm^3/hr.

This research explores the design rules for MBAAM, which are driven by the process resolution and overhang constraint. Building on an angle with additive manufacturing results in a stair stepping effect, as shown in Figure 1. The overhanging portion of the layer bends under its own weight, and subsequent layers deposited on top of the bending material can result in a build failure. Typically, support structures are used to span the overhang and reduce material bending. The supports are easily removed by hand or dissolved in water, depending on the process used, when the part is completed. Each AM process and material combination has its own maximum overhang length, although most processes use a 45° overhang as the standard to apply supports. However, MBAAM cannot deposit easily removable supports. MBAAM only deposits the full strength metal it is using, so post processing is needed to remove any supports; as a result, the use of supports is avoided in MBAAM.
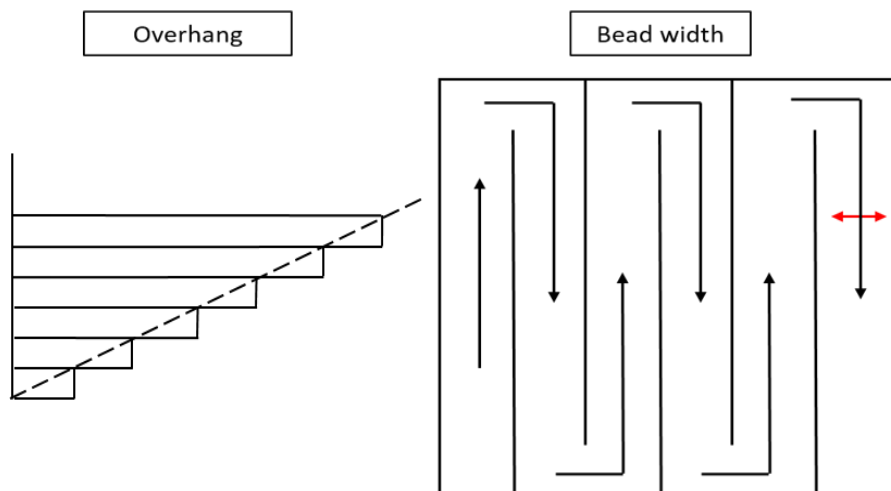
Figure 1. Overhang (left) and bead width (right).

Process resolution for MBAAM considers both the bead width and thickness. The bead width is shown in Figure 1 by the red arrow, and the black arrows show a raster toolpath.

For MBAAM, the high deposition rate is made possible by lower resolution, represented by a wider bead. As is the case for all AM, structures have to be designed in multiples of the bead width. The bead width for MBAAM is nominally 6mm, which is on the order of many thin wall plate structures that are good candidates to be replaced by an MBAAM part. This proves to be a challenge for the enclosed excavator arm case study, where the nominal plate thickness for the arm is 8mm.

One method to reduce the weight of an arm using thicker plates is to use topology optimization. Topology optimization is used in this study to find the optimal locations and sizes of holes in an excavator arm modified to have 12mm thick walls. However, the actual implementation of the optimization results is still subject to the MBAAM process design rules, so the printed arm does not take full advantage of the weight reduction.

The overhang constraint and process resolution limit certain geometric features that are required for structural components, such as mechanical interfaces and cutout holes for weight reduction. As such, "printable" is a term used to describe whether a given geometrical feature meets the design rule requirements. Geometric features for MBAAM are classified as: features that are printable as-designed, features that require modifications to be printable, and features that must be fabricated via post process operations (*e.g.*, machining).

These feature types are presented using a case study in re-designing a 5.5 ton excavator arm for fabrication using MBAAM. The excavator arm is an excellent demonstration of additive manufacturing as the construction equipment industry routinely uses equipment past its intended lifetime, and sometimes replacing a part on a legacy machine is impossible

since the original manufacturer no longer has the tooling to make a replacement. A replacement part is made by regenerating the original tooling for the part. A future alternative is to redesign and fabricate the component using additive manufacturing techniques such as MBAAM. This thesis demonstrates that producing such a replacement with no tooling via additive manufacturing is viable, and that future efforts can decrease the design and fabrication time for a replacement part to as short as several weeks.

The final printed excavator arm displays examples of the feature types explained in the previous text. The methodology for deciding to modify or omit features from the printed design is discussed. Cutout holes for weight reduction are generated using topology optimization and then integrated and modified using the design rules. Finally, due to the geometric changes in the arm, a structural analysis of the final arm geometry verifies that the component has sufficient strength to avoid failure under expected loading.

The remainder of this thesis describes the design process for the excavator arm. A literature review of additive manufacturing, welding, and topology optimization is presented in Chapter 2. The design rules, geometry feature designation, and finite element analysis setup are discussed in Chapter 3. The results of the finite element (FE) analyses and the printed part are presented in Chapter 4, followed by a discussion on the wider contributions of this project. The conclusions are presented in Chapter 6, followed by recommendations for further research investigations in Chapter 7. The appendices present more FE results and a derivation of the topology optimization algorithm.

CHAPTER 2. BACKGROUND

This chapter presents a literature review of additive manufacturing, welding, and topology optimization. The literature review provides background for understanding the relationships between structure, process, properties, and design in MBAAM.

2.1   Additive Manufacturing

From a broader standpoint, additive manufacturing refers to any manufacturing process that adds, rather than removes, material. In this thesis, though, additive manufacturing refers to accumulating layers of material to build a three dimensional object. This section describes common AM processes in polymer and metal applications.

Each additive manufacturing process has its own set of design rules based on the physics of the process. Layered manufacturing offers more design complexity freedom than traditional casting and machining, but there are limitations. Process resolution and support structures are the driving limitations for additive manufacturing. Material built on an angle bends under its own weight like a cantilever beam, and subsequent layers compound the geometric errors. Support structures prevent the bending and provide a surface sufficiently flat to deposit on. An example of support structures is demonstrated using an example from FDM in Figure 2. Sacrificial material is added to provide material to deposit on top of. This material can be easily broken away or dissolved. As shown in the figure, though, changing the print direction can eliminate the need for support structures for certain geometries.
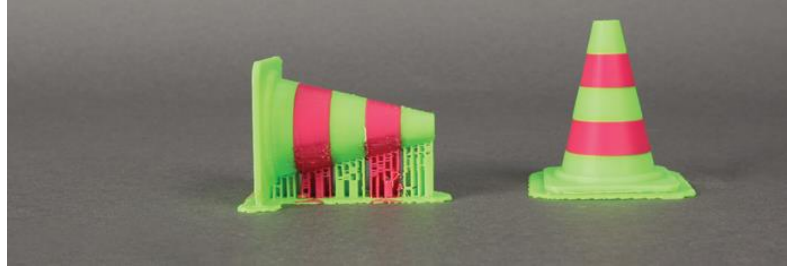
Figure 2. Overhang demonstration, from [1].

2.1.1 Polymer Additive Manufacturing

Polymer AM is recognized as being introduced by Charles Hull in 1982 as stereolithography (SLA) [2]. Layered manufacturing of polymers and polymer-matrix composites now includes a variety of polymers and deposition techniques [3]. The most common polymers are acrylonitrile butadiene styrene (ABS), polylactic acid (PLA), and nylon, which can be combined with fibers or whiskers to increase strength and ductility. The most common methods for fabricating polymer 3D components are photopolymerization, used in stereolithography (SLA); extrusion deposition, used in fused deposition modelling (FDM); and sintering, used in polymer selective laser sintering (SLS).

2.1.1.1 Stereolithography

Stereolithography uses laser light to photopolymerize a thin layer of resin at the surface of a vat of uncured liquid resin. As shown in Figure 3, the stage moves down in the z-direction and a wiper blade spreads a uniform layer of uncured resin on top of the part. Commercial systems have demonstrated, at their highest resolutions, Z resolution (the layer thickness

in the print direction) of 0.051mm and X/Y (in the build plane) resolutions of 0.102mm

over the length of the build volume. The difference in resolution between the build plane

and print direction is due to shrinkage in the X/Y directions [4]. Tensile strengths are on

the order of 55 to 70 MPa [5], but mechanical strength of the polymer deteriorates in UV

light. Thus, SLA parts are used more for molds and tooling than end-use parts [6]. Build

volumes extend from 100mm x 100mm x 100m for a desktop hobbyist system to 800mm

x 330mm x 400mm for an industrial system. The build rate is on the order of 1-3 cm/hr in

the z-direction [7]. Supports are used in SLA to extend the usable overhang angle to 45°.

The support material is simply a thin cylinder of the same resin built up to meet the part's

overhanging surface.
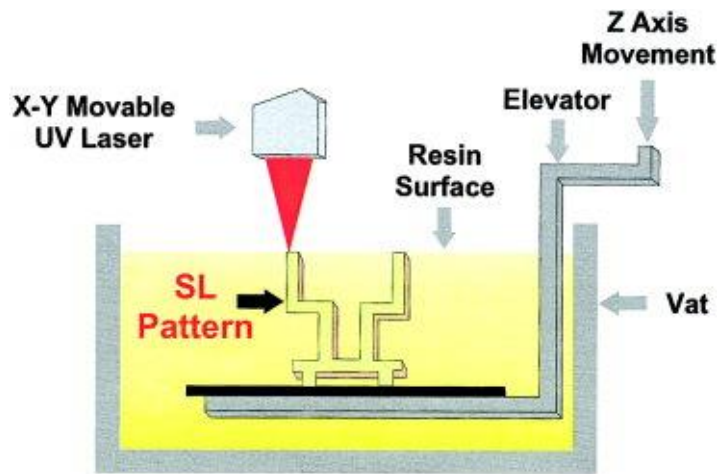
**Figure 3. Schematic of stereolithography process. The elevator moves in the vertical
direction in increments on the order of microns. From [8].**

2.1.1.2   Fused Deposition Modelling

Fused deposition modelling (FDM) uses polylactic acid (PLA) or acrylonitrile butadiene

styrene (ABS) filament to quickly fabricate hobbyist and prototype models. The

maximum feature resolution for FDM is on the order of 100 μm [8] and the accuracy over

an entire part is ±0.15% with a lower limit ± 0.2 mm for a professional grade FDM

system [9]. Surface roughness ranges from 5-30 μm [10], and is dependent on the process

parameters such as viscosity of the polymer melt and width of the deposited polymer

bead. A diagram of an FDM printer is shown in Figure 4. FDM systems typically make

use of thin, low strength support structures out of ABS that can be removed by hand or

with pliers.
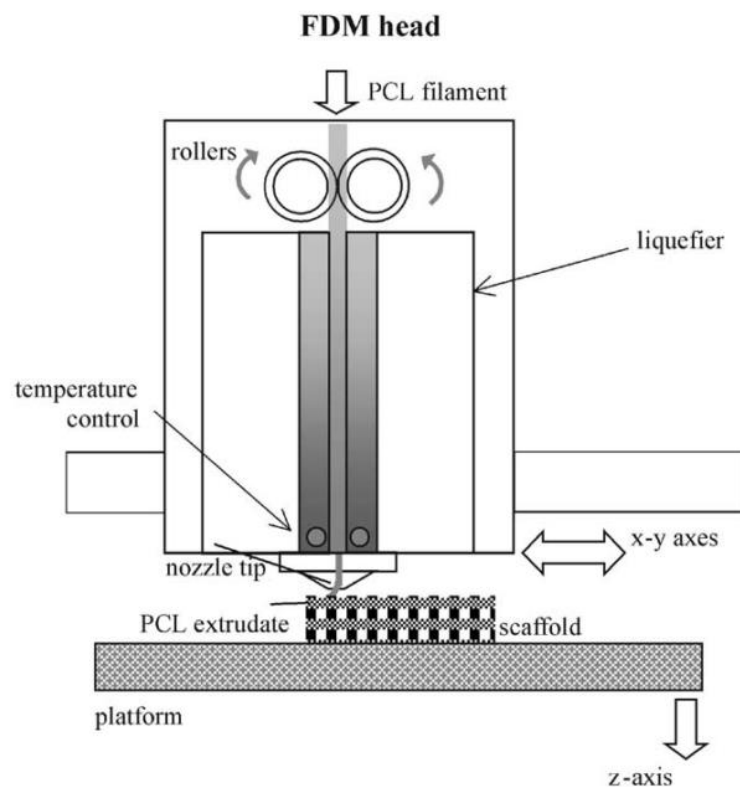
Figure 4. FDM diagram from [11].

The mechanical properties of a part fabricated by FDM depend on the deposition

strategy, bead width, and deposition temperature, among others [12]. The tensile strength

of FDM using ABS ranges from roughly 11 MPa to 25 MPa [12]. Build rates for FDM

range from 15-85 cm^3/hr [13], and build volumes range from a desktop machine of

152mm x 152mm x 152mm [14] to 914.4mm x 609.6mm x 914.4mm on an industrial-quality system [15].

2.1.1.3   BAAM

Big Area Additive Manufacturing (BAAM) represents the most successful large scale polymer AM system currently available. BAAM uses a custom FDM extruder to fabricate very large components, such as the world's first 3D printed car, shown in Figure 5. The ABS used in BAAM is strengthened by adding chopped carbon fibers [16]. The build volume is currently 6m x 2.3m x 1.9m, but the build volume is ultimately dependent only on the size of the gantry the extruder is attached to. The deposition rate, assuming a 20% carbon fiber backfill, has a maximum rate of around 39,000 cm^3/hr. Its resolution is determined by a bead width of 8.4 mm and a thickness of 4 mm [13].

Figure 5. Strati developed by Local Motors in partnership with ORNL. From [17].

Overhangs in BAAM can be supported using break away support structures. These structures prevent printing over free space. BAAM has an overhang limit of 45-50° off the vertical print direction before break away support structures need to be added, and the support structures extend the overhang limit to 70-72° [18]. The mechanical properties are

anisotropic, with a tensile strength of 53 MPa in the build plane and 18 MPa in the build direction when using 13% backfill ABS/CF [13].

2.1.1.4   Polymer AM Design

Polymer additive manufacturing does not have sufficient resolution to print mating surfaces needed for assembly such as screw threads and bearing sleeves. While printed hinges [19] and shafts and gears [20] have been demonstrated using FDM, they are not useful for functional parts. The required clearances for printed FDM parts are higher than those needed in machining, since the average surface roughness is much lower in machining. In the article on the printed shaft, a non-peer reviewed study, it is reported that a shaft made with FDM would need a radial clearance of 0.25-0.3 mm with ABS or nylon and 0.15-0.2 mm with PLA, while a machined shaft would need a radial clearance of 0.05 mm [20].

An assembly that needs fasteners will require post processing to add threaded holes and bearing sleeves. The X/Y resolutions of both SLA and FDM are on the order of 100 micrometers, and classes of fit for threaded holes have an X/Y resolution of 12.7 to 88.9 micrometers. A functional part made using FDM or SLA should thus use hand-tapped threads and standard screws.

BAAM requires post process machining for smooth surfaces and mechanical interfaces for functional parts. The deposited polymer beads are wide enough to require decisions on printing features or implementing them in post processing. The rough surface is smoothed by a 5-axis CNC router, which then permits painting or other cosmetic adjustment. A CNC router is appropriate because machining ABS/carbon fiber composites does not require heavy duty power found in other CNC machine tools.

Polymer AM offers a range of design complexity, where through a combination of support structures and process resolution, complexity is free. Functional parts in polymer AM are in use in real world applications, but polymer AM parts are not suitable for a range of structural applications such as high strength, high temperature, and high contact wear scenarios.

2.1.2   Metal Additive Manufacturing

Metal additive manufacturing has been used to fabricate complex components for demanding applications such as jet engine nozzles, customized orthopedic implants, and topology optimized aerospace brackets. These geometries are unable to be fabricated by any other manufacturing process. Additionally, alloys that are difficult to machine, such as titanium and nickel alloys, are suitable to additive manufacturing, since they are weldable. This section describes the metal AM processes: Laser Engineered Net Shape (LENS), Selective Laser Melting (SLM), and Electron Beam Melting (EBM). Materials, strength, and surface roughness will be discussed for these processes.

2.1.2.1   Laser Engineered Net Shape

The LENS process was developed at Sandia National Laboratories in the 1990s [21], [22]. It feeds a stream of atomized metal powder into a high power laser beam to melt and fuse the powder to the work below, as shown in Figure 6. The mechanical properties for 316L stainless steel samples fabricated via LENS include 410 MPa for yield strength and 640 MPa for tensile strength. With heat treating, the measured properties become 340 MPa for yield strength and 610 MPa for tensile strength. The mechanical properties compare well to cast and wrought (cold finished) 316L stainless steels. Properties for these samples have

yield strengths of 262 MPa and 280 MPa and ultimate strengths 552 and 574 MPa, respectively [23], [24]. The arithmetic surface roughness of a LENS sample using Inconel 690, a nickel-base superalloy is ~12 μm and the deposition rate is approximately 2.215 cm^3/hr [25]. The dimensional accuracy over the entire part can be maintained at ± 0.02 mm in the horizontal direction and maintained at ± 0.4 mm in the build direction [26]. The bead geometry is controlled by the laser power and translation speed, with bead widths between 0.6 mm and 2.4 mm and layer thicknesses between 0.2 mm and 0.8 mm [27]. Commercial machines for LENS have build volumes ranging from 100mm x 100mm x 100mm to 900mm x 1500mm x 900mm [28], [29].
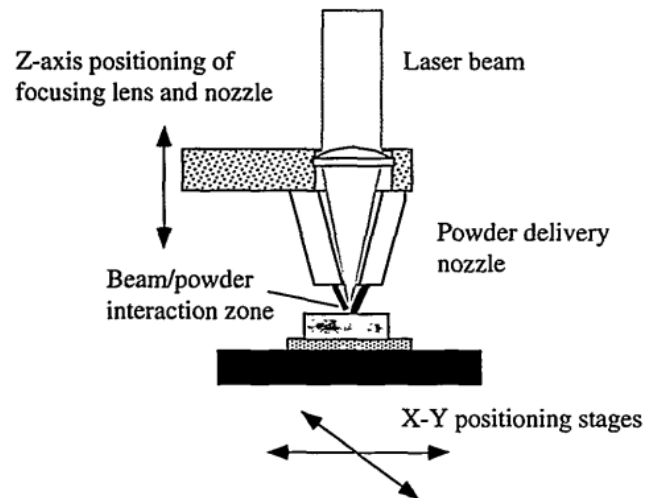
Figure 6. Schematic of LENS process, from [30].

2.1.2.2   Selective Laser Melting

Selective Laser Melting (SLM) uses a scanning laser to melt and fuse successive cross sections in a powder bed of metallic alloy. SLM has a related process called selective laser sintering (SLS), but SLS is not considered in this thesis because the parts require firing in

an oven to come to full strength and density. SLM parts are stronger but have higher residual stresses and a rougher surface finish due to the temperatures needed for full melting [31], [32]. SLM uses easily removable, thin support structures to create complex geometry.

Selective laser melting fully melts the powdered metal, although a heat affected zone surrounds the solidified bead in the unmelted powder. Vrancken et al. reports that mechanical properties for the selective laser melting of Ti-6Al-4V are a yield strength of 1,110 MPa and an ultimate strength of 1,267 MPa [33]. A reference sample in reported in the same paper has a yield strength of 960 MPa and an ultimate strength of 1,006 MPa. The difference in properties is likely due fast cooling rates in SLM yielding small grain size. The surface roughness in SLM suffers from partially melted powder sintered to the surfaces, with roughness values for a stainless steel 316L sample between ~8-17 μm [34]. Selective laser melting has build rates from 25 cm^3/hr on a 125 x 125 x 125 mm^3 machine, and a build rate of up to 120 cm^3/hr in the largest of machines with two lasers and a build volume of 800 x 400 x 500 mm^3 [35].
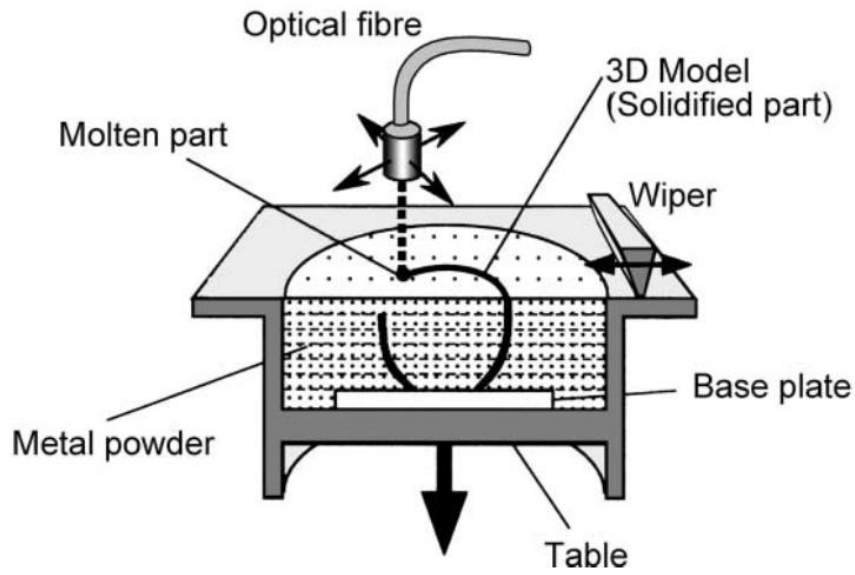
Figure 7. Selective laser sintering/melting example schematic. From [36].

2.1.2.3 Electron Beam Melting

Electron beam melting bombards the surface of a powder bed with a focused flux of electrons to melt and fuse cross sections of a 3D component. It uses a powder bed similar to the selective laser melting process, but the entire layer is sintered in a pre-heat scan by de-focusing the beam and rapidly moving across the surface before fully melting the desired cross section with a focused spot size. A diagram showing the electron beam gun and powder bed is shown in Figure 8. The use of support structures is optional [37], since the sintered powder can provide a base to build from.

EBM provides mechanical properties similar to SLM, but with higher elongation and lower yield and ultimate tensile stresses. The difference in mechanical properties can be attributed to the higher cooling rates in SLM [38]. The build rate for EBM is on the order of 60-80

cm^3/hr with an accuracy of ± 0.20mm over 100mm, and the build volume for a popular

commercial machine is on the order of 250mm x 250mm x 400mm [39],[40].
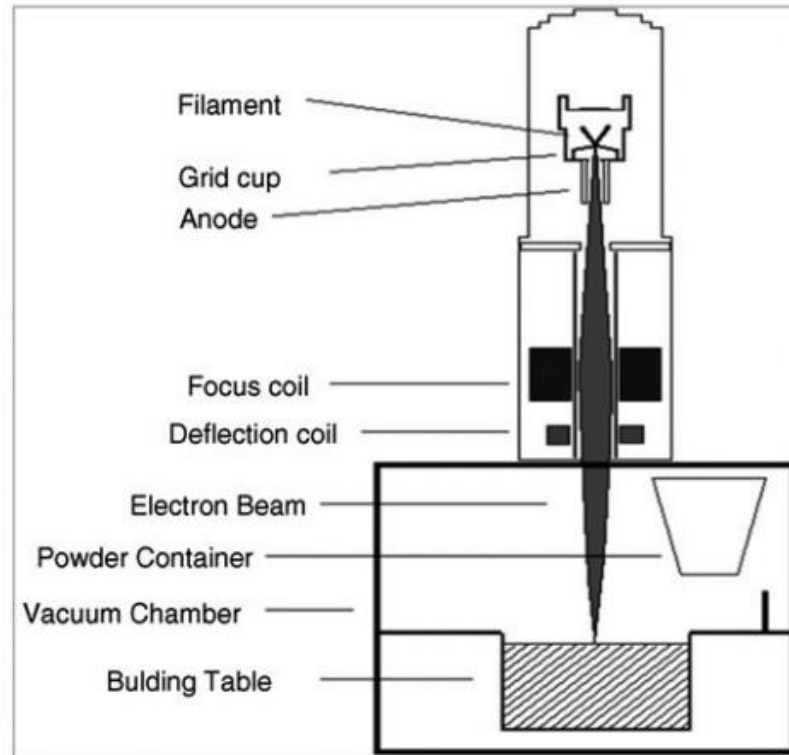
Figure 8. Schematic of the electron beam melting process, from [9].

2.1.2.4   Metal AM Design

Metal AM processes are near net shape processes similar to castings. One advantage of

AM is that the part count for a functional part can be reduced by combining parts that

would typically be fastened into an assembly. A pilot hole can be printed where needed,

with post-processing drilling to bring the hole to specification.

Metal AM processes using powder require post processing to remove the partially melted

and sintered powder on the surfaces. Additionally, any internal geometries such as cavities

will be filled with unmelted powder and will need a drainage hole to remove it. Any surface not needed for aesthetics or assembly can be left as is.

2.2   Metal Big Area Additive Manufacturing

The Metal Big Area Additive Manufacturing (MBAAM) process increases build volume and deposition rate by using wire instead of powder. The first reported metal additively manufactured component dates back to the 1960s when Krupp and Thyssen fabricated a 5.79 meter diameter by 10.36 meter long cylindrical pressure vessel using a submerged arc welding process [41]. The arc weld deposition process used in MBAAM has its origins in the late 1980s at Babcock and Wilcox Co. [41], but it has not seen widespread acceptance in industry yet due to the superior dimensional accuracy of powder bed processes described above such as EBM and SLS/SLM.

Design for MBAAM is governed by the overhang limit and lack of easily removable support structures. The overhang limit is due to the fact that the tool orientation is always normal to the cross sectional layer, and thus the molten metal can run off the top layer if the overhang angle is too high and if the substrate is too hot. The substrate temperature plays a role in the viscosity of the melt pool, with higher temperatures resulting in lower viscosities. Low strength, easily removable support structures are not feasible in MBAAM. Any supports are full strength steel, at least in the current situation, with the nominal bead thickness. Thus, minimal support or support-free geometry is recommended. The design rules for MBAAM are discussed further in Chapter 3.

ORNL has developed an in-house solution for generating the toolpath in the BAAM and MBAAM systems. The software does not have automatic overhang detection, so the

operator determines if an overhang is feasible. Further details of the toolpath generation software operation are not discussed in this thesis.

The MBAAM concept is based on the gas metal arc weld (GMAW) deposition of steel filler wire. Thus, the GMAW process must be fully understood to know the limitations therein. This section will discuss the fundamentals of arc welding and how they pertain to MBAAM.

2.2.1 Gas Metal Arc Welding Equipment

MBAAM is based on Gas Metal Arc Welding (GMAW). Other wire-fed additive manufacturing processes use Gas Tungsten Arc Welding (GTAW) [42], lasers [43], electron beams [44], and plasma [45]. The choice of alloys spans the range of weld-able metals, though titanium alloys, carbon steels, and nickel-based superalloys have been studied the most. Mechanical properties largely approach the bulk properties of the alloys, and the rate of deposition is much higher than with powder bed or powder-blown processes [46].

Arc welding uses an electric arc to melt and join metals. An electrode is clamped to the workpiece, leading back to the weld head. The weld torch acts as the other electrode to make the electrical connection. In the case of GMAW, the filler wire is a consumable electrode. This differs from the gas tungsten arc weld (GTAW) process, which uses a non-consumable tungsten tip for the electrode and the filler wire is fed in from the side. Figure 9 below shows the electrical connections necessary for arc welding.

Molten metals and alloys require shielding from surrounding oxygen to ensure a clean weld. Stick and flux core welding use a "flux" layer on the welding rod to keep oxygen out of the welds. GMAW, GTAW, and laser welding use shield gas to prevent air from oxidizing the molten metal in the weld pool. The shield gas is selected based on the alloy, with some metals requiring a fully inert environment such as argon, and others needing a mixture of argon and carbon dioxide. Electron beam welding is performed in a vacuum to prevent deflection by air or any other gas molecules.
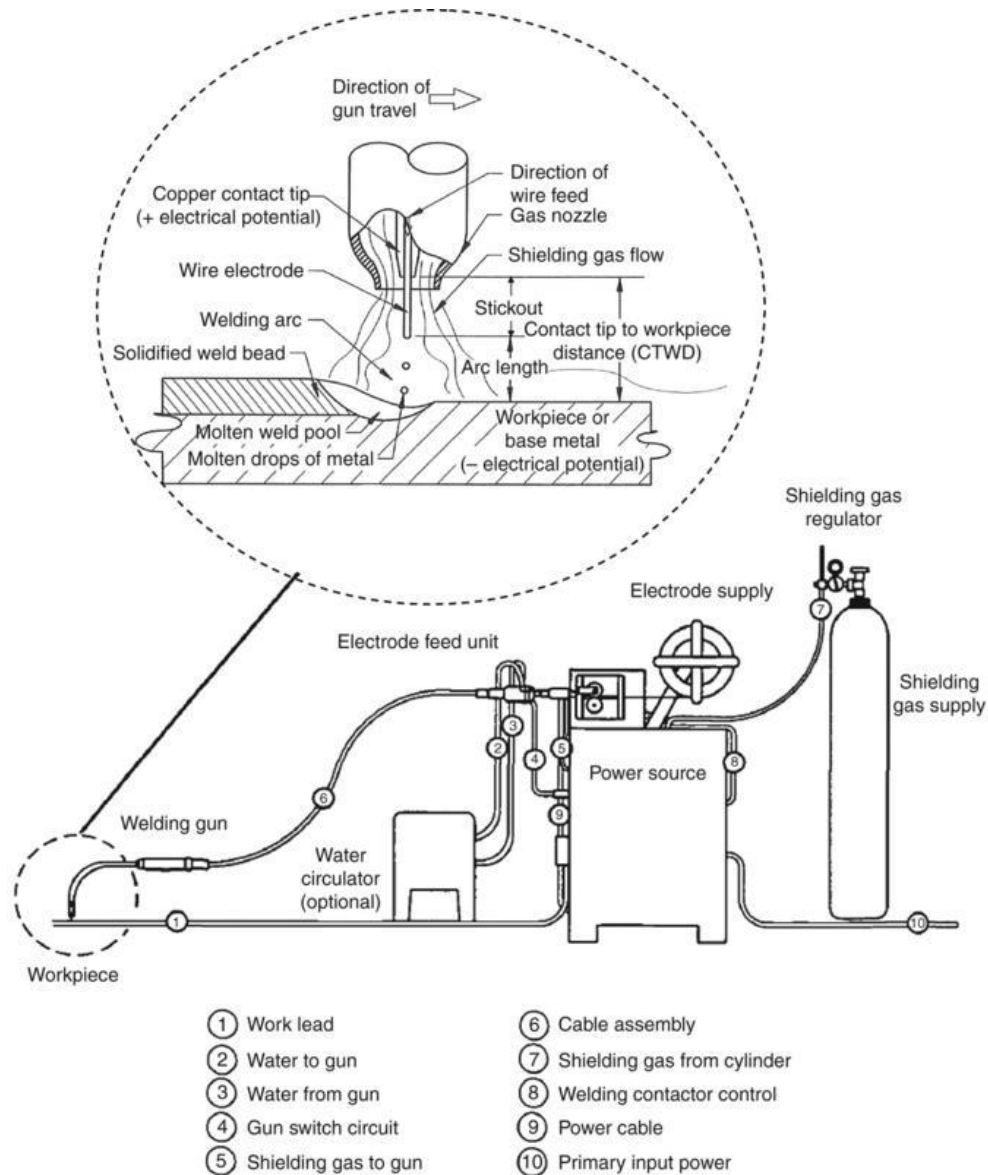
Figure 9. GMAW operation. From ASM Vol 7 [47].

2.2.2   Heat Flow

The flow of heat in welding is plays a large role in the weld's structure-property-process

relationship. Heat transfer through the weld pool to the parts being joined determines to

the weld's microstructure, residual stress, and distortion. Cooling rates, inter-pass

temperatures, and weld bead sequencing all play a role in the thermomechanical history of

19

a weldment. This section discusses some of the process variables and their effects on the resulting weld, and how the heat transfer problem is extended to AM.

The heat input in a weld is a function of applied voltage and current and weld torch travel speed. A simple heat input model is

$$\frac{VI}{S} \qquad (1.)$$

where V is the voltage, I is the amperage, and S is the torch speed. The units of heat input are energy per unit length, and this heat input determines the properties of the weldment. A diagram of the fusion zone, heat affected zone, and base metal is shown in Figure 10. The heat affected zone is the region outside of the fusion zone, but close enough to undergo thermal cycling-induced grain refinement and solid state phase transformations, thus changing the weld metal's mechanical properties. The hardness and fracture toughness of the weld metal and heat affected zone decreases with increasing heat input [48]. In the base metal, increasing the heat input will result in larger grains; likewise decreasing the heat input will result in smaller grains [49].
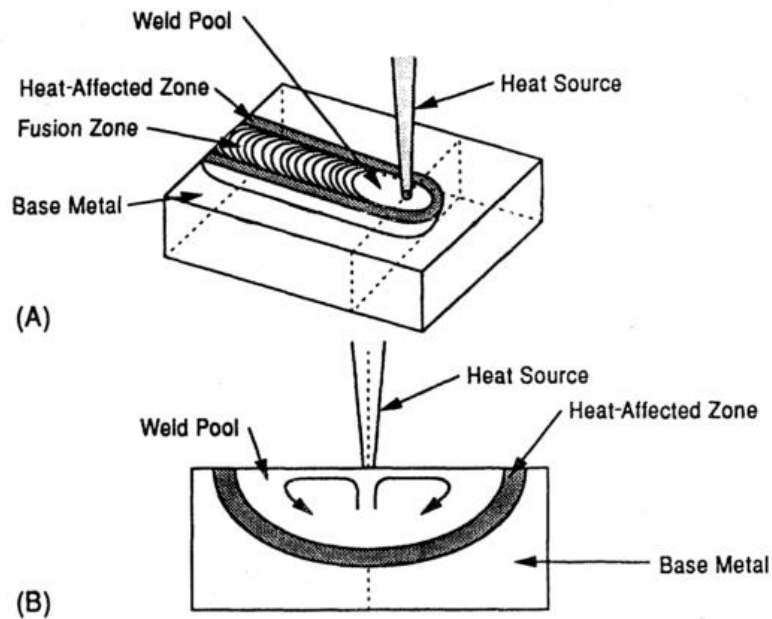
Figure 10. Schematic showing the weld pool, HAZ, fusion zone, heat source, and base metal. From [50].

Studies of mutli-pass welding, which is fundamentally similar to MBAAM, have shown that lower layers in the build are annealed by the thermal cycling, with the maximum hardness at the top layer decreasing the minimum hardness at the bottom layer [42]. This is further extended through showing that the time spent between 800˚C and 500˚C (also denoted t_{8-5}) has been identified as a crucial parameter in fracture toughness of steel welds. For example, the maximum fracture toughness in a High Strength Low Alloy (HSLA) steel is shown to be highest when the time to cool from 800°C to 500°C in a simulated weld cycle is 18 seconds [51].

The substrate temperature has a large effect on the deposited bead geometry. If the work's temperature is too low, the bead will be too narrow and too high. Further, if the work's temperature is too high, the weld pool behavior is random and has been observed

to flow off of the top of the layer [52]. The tendency of the bead to overflow is thus a combination of the substrate temperature and heat input to the bead and substrate. The heat input has a range where there is enough energy input to fuse the bead and substrate together, but not too much to cause the substrate to melt too much and cause overflow. This emphasizes the importance of the processing parameters on the resulting structure and properties of the finished component.

Thermal simulations can predict these parameters for metal AM. To date, simulations of $t_{8\text{-}5}$ and substrate temperatures to prevent overflow have not been used to generate toolpaths for MBAAM. The thermal simulations have been established for similar processes, though, as demonstrated by the calculated temperatures for 10 layers of weld-based steel deposition shown below in Figure 11.
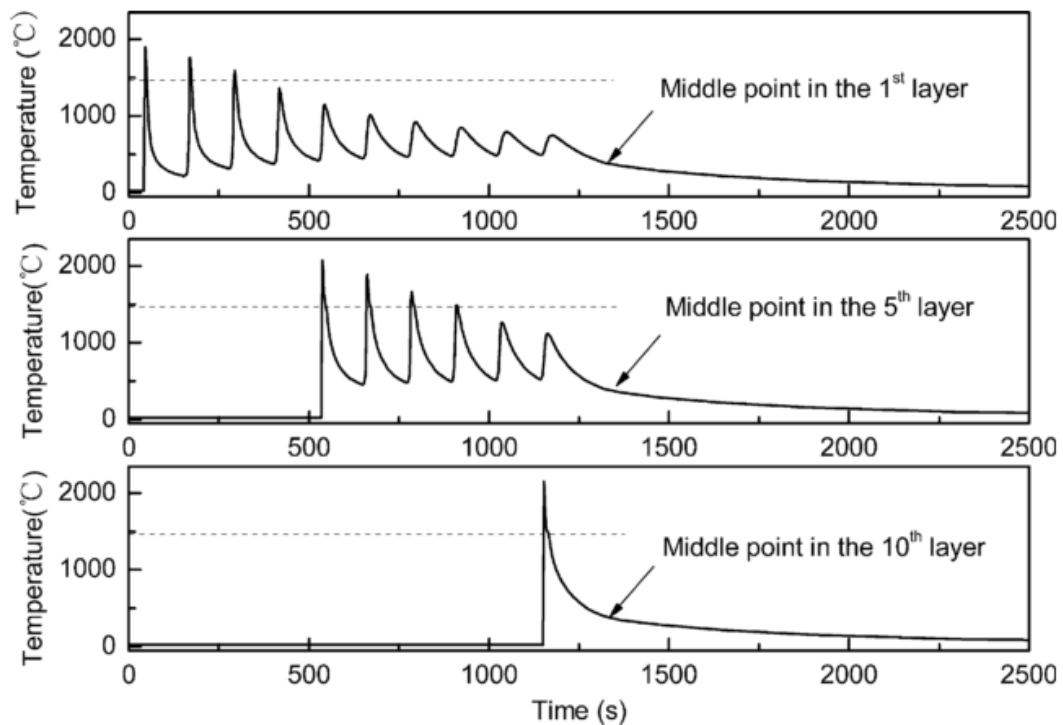
Figure 11. Calculated thermal history of weld deposition. From [42].

Welding on cold metal produces a thicker initial bead than when the substrate is hot. This bead geometry difference can lead to geometrical errors in a part built using MBAAM. The resulting bead thickness changes from the uncontrolled substrate temperature are considered by the toolpath generation software package. From empirical results, the first three beads are assigned different thicknesses from the steady state bead thickness. If a build is allowed to cool overnight before restarting the next day, the first few beads will be thicker than intended. This produces a finished part that will not be to the intended specifications. Subsequent post-processing and assembly may suffer from misfit in the part geometry.

2.2.3 Defects

Defects in welding can come from many different sources. Solidification cracking in the weld joint occurs when new, lower volume solid phase at the interface of the weld pool cannot resist the contraction of the cooling and solidifying weld metal. Higher weld speeds lengthen the weld pool, thus a greater portion of the weld pool is at risk for cracking [53]. Alloy impurities also increase the susceptibility to cracking. In stainless steel, for instance, the fusion zone microstructure needs 5 to 15% by volume delta ferrite to resist cracking from sulphur and phosphorus [54], [55].

The limit for deposition rate in MBAAM is the same as for GMA welding. Weld pool hydrodynamic instability is a dominating factor for determining the speed limit for GMAW. When the torch speed is too high, the liquid bead is too thin, and surface tension forces pull the continuous, even bead into the shapes shown in Figure 12 [56], [57]. Multiple heat sources have been shown to control the formation of bead "humping", and allows the weld speed to increase by a factor of 2 or 3 [58]. These tandem heat sources can include GTAW-GTAW, GMAW-GTAW, GTAW-laser, and multiple lasers.
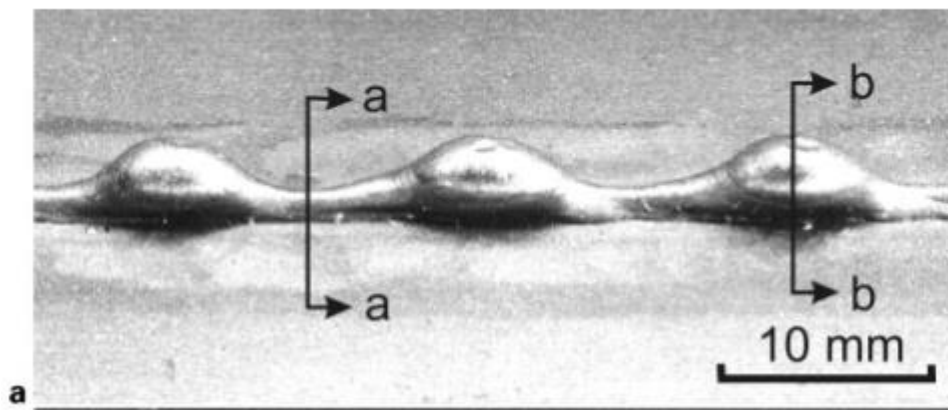
Figure 12. Defects in welding at high torch speeds is hypothesized to be due to instability in the weld pool. From [13].

2.2.4   Residual Stresses

The applied thermal gradients in welding and MBAAM induce residual stresses from nonuniform heating and cooling. Residual stresses form when the thermal stress surpasses the yield strength of the weld metal and some of the surrounding heat affected zone, inducing plastic strains. Upon cooling, the permanently stretched metal is compressed by the elastic unloading of surrounding material. In metal additive manufacturing, residual stresses from depositing hot material onto a colder substrate can cause delamination and cracking from the sudden thermal expansion of the substrate relative to the layers further below it. Residual stresses can be controlled through stress relieving processes such as heating the opposite side of a weldment with a torch to introduce opposing residual stresses or post weld heat treatment [59].

Residual stresses can also be reduced by sequencing the welds based on computational predictions of residual stresses. The sequencing can be optimized by heuristic methods such as genetic algorithms. Park and Lee showed that genetic, simulated annealing, and tabu search algorithms could all be used to find the tool path that avoided including the HAZ of one weld bead in the path of another bead until the first bead had time to sufficiently cool [60]. Lostado-Lorza et al. have combined genetic algorithms with model trees, a data mining technique, to improve the effectiveness of path optimization [61]. The problem of weld sequencing optimization has not received much attention in the literature, but that is subject to change with weld-based deposition additive manufacturing techniques now gaining popularity.

2.2.5   Deposition Rate and Feature Definition

Deposition rates in wire feed AM are inversely related to geometric accuracy, as shown in Figure 13 [62]. Arc weld deposition rates have been reported between approximately 150 cm^3/hr and 500 cm^3/hr for other additive manufacturing processes [63]. Higher deposition rates can be achieved using a second heat source. Hot wire GMA welding can increase speeds by 2 to 3 times, and hybrid laser + arc welding or GMA + GTA welding similarly increase the welding speeds.
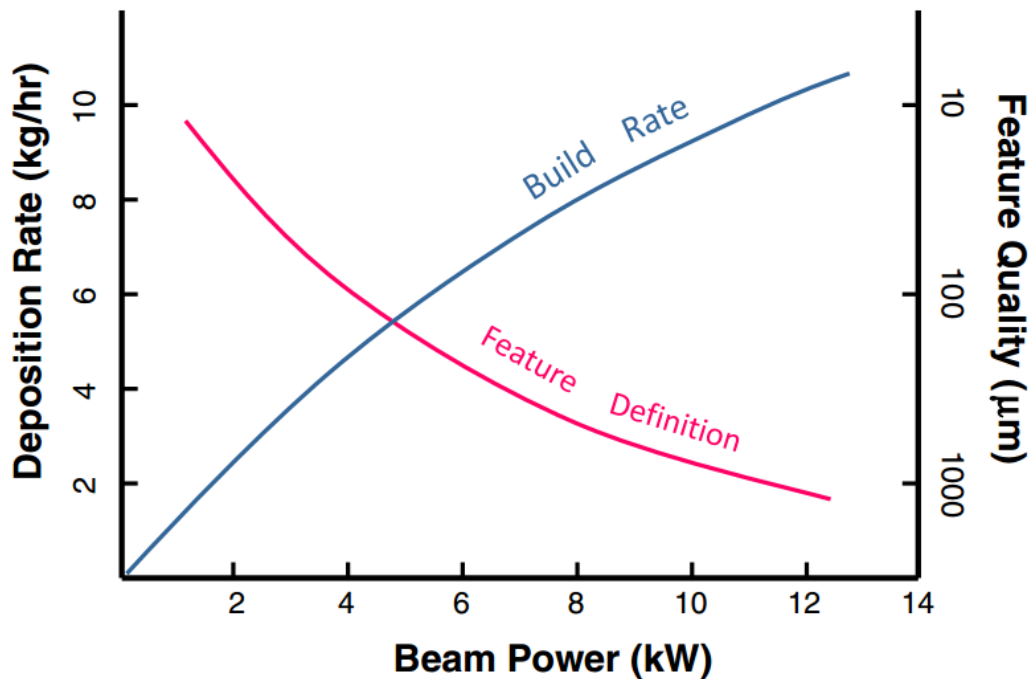
Figure 13. The inverse relationship between build rate and feature definition. From [62].

Due to the inverse relationship between deposition rate and resolution, the geometric accuracy can be increased by using a machining operation after printing to achieve a smooth, uniform surface. Machining is a cutting process that has high accuracy and precision. A limiting factor for using machining after arc weld deposition is the tool accessibility. Inside surfaces will not be accessible for post processing; a hybrid

26

additive/subtractive system utilizing machining in-process is an alternative to reach the inside surfaces.

2.3   Summary of AM Processes

The use of additive manufacturing to produce functional parts has become more widespread due to increased reliability, ease in fabricating complex designs, mechanical strength, and established design rules. However, some features cannot be printed. Mating surfaces need to be brought to the final dimensions with post processing machining, drilling, etc. Additionally, while the dimensions and tolerances of parts intended for fabrication with conventional methods can be adjusted to suit AM processes, using additive manufacturing to its fullest capability requires re-designing the part to combine functionality such as load-bearing heat sinks, or embedded electronics. The re-imagining of a product for fabrication with additive manufacturing is most effective when designing for the intended process.

Selected processes listed in the text above are summarized in Table 1 below. The "Representative Application" column shows some of the representative objects made with the process. The "Material" column is not exhaustive; new materials are constantly in development. The table is intended to give perspective on how the large scale AM systems, BAAM and MBAAM, compare to the other AM processes. BAAM decreases the material cost by a factor of 16 and dramatically increases the build volume and deposition rate. MBAAM decreases the material cost by a factor of over 101, and the build volume and deposition rate are increased, but not to the extent of BAAM.

Table 1. Summary of AM Processes.

Process	Material	Build Volume	Material Cost	Deposition Rate	Representative Application
FDM	ABS	5660 cm^3	ABS Filament $176/kg	15-85 cm^3/hr	Yoda Head
BAAM	ABS/Carbon Fiber	7.9e6 cm^3	CF-ABS Pellets $11/kg	39,000 cm^3/hr	Car
Metal Powder Bed	Ti, Ni, Stainless, Al	8500 cm^3	Atomized Ti-6Al-4V Powder $1,323/kg	60-80 cm^3/hr (EBM)	Aerospace brackets
MBAAM	Steel, Al	>1.1e5 cm^3	Steel Filler Wire $13/kg	< 640 cm^3/hr	Mini excavator arm

2.4   Topology Optimization for Additive Manufacturing Design

Additive manufacturing facilitates designs that cannot be made by any other manufacturing processes. Using material more efficiently, such as using less raw materials to design a structure that meets safety requirements, is a common goal for design engineers in additive manufacturing. Computational tools are being developed to generate concepts for structural optimization. Analytical optimization techniques exist to optimize problems such as the cross sectional areas of trusses, but analytical techniques are insufficient for continuum solid structures. For continuum structures, the finite element method has been combined with optimization techniques to find the optimal material distribution in a volumetric design space; this technique is called topology optimization.

The basic minimization problem is described as minimizing an objective function subject to a set of constraints:

$$\min_{x} f(x) \tag{2.}$$

Subject to

$$g_i(x) \leq 0$$

(3.)

$$h_i(x) \leq 0$$

Where x is the vector of design variables, $f(x)$ is the objective function, and $g_i(x)$ and $h_j(x)$ are constraints. The constraints shape the feasible domain space to better represent the problem at hand, such as a minimum radius in a truss or a minimum volume in a continuum problem. A typical topology optimization problem needs multiple constraints to make the optimization meet certain requirements, like manufacturability, feature size, or hole formation.

2.4.1 Types of Optimization Algorithms

Gradient-based algorithms for topology optimization such as the Method of Moving Asymptotes (MMA) was introduced in 1987 [64]. Later methods such as projection [65], [66], level set [67]–[69], and phase field [70] techniques were introduced in the 2000s. Bi-directional evolutionary structural optimization (BESO) is also common in real-world applications [71]. These methods are all alternative methods to find the sensitivity of the discretized objective function and can be combined with material interpolation algorithms such as SIMP [72] or RAMP [73] to avoid numerical instabilities in the solution. These algorithms have all proven to be robust and are efficient optimization technique when the problem is properly posed.

Genetic algorithms (GAs), which do not use gradients to select the next iteration in the optimization algorithm, have been shown to be inefficient for topology optimization [74]. GAs introduce random variations to test, rather than following the path of steepest descent. GAs have been effectively used in analytical structural optimization problems [75], but the millions of elements involved with continuum, solid structures makes GA techniques slower, since many more iterations are needed when compared to gradient methods. Likewise, analytical techniques, which have their roots in Michell's 1904 paper on minimizing the amount of material used in a truss system [76], are inappropriate to use in the continuous material distribution problem at hand.

2.4.2 Compliance Minimization

The most common topology optimization problem is that of compliance minimization, or equivalently, stiffness maximization. The goal is to minimize the overall compliance of the structure subject to a constraint, typically the volume of the structure. This is in contrast to the more intuitive approach of minimizing mass subject to a maximum allowable stress. However, the mass minimization problem is more complex to implement in finite element analysis than compliance minimization, so to-date, commercial codes only offer the compliance problem.

Compliance minimization is converted into a convex optimization problem using the MMA algorithm, but SIMP reverts it to a non-convex problem when the penalization value is too aggressive, causing instabilities [77]. When the penalization exponent is 4 or more, the risk for numerical instabilities in the solution rises. An example of a numerical instability is shown below in Figure 14. The beam problem is shown in a) and b) shows the checkerboard

numerical instability when the penalty parameter is too high. C) is an example of a low fidelity mesh, and d) is the result when using a high fidelity mesh with the proper penalty value.
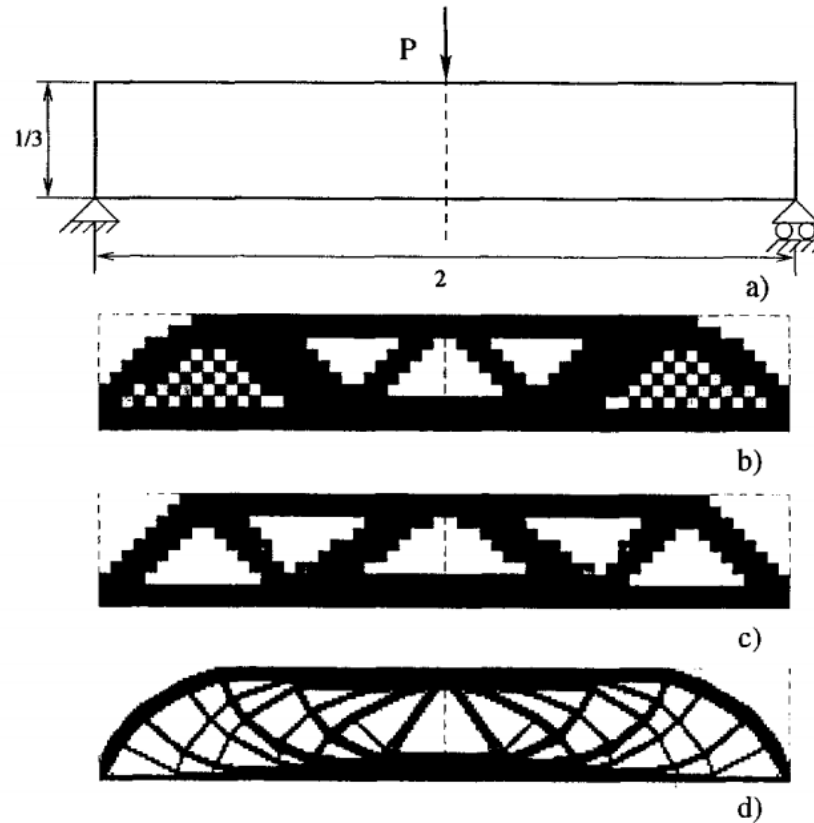
Figure 14. Checkerboard instability in topology optimization. From [78]**.**

2.4.3   Optimization Considering Manufacturing Constraints

Topology optimization is considered a design concept generation tool, but even if adjustments must be made to the resulting geometry, curtailing the feasible domain is critical to making geometry that can be fabricated. Manufacturing-tolerant constraints have been demonstrated for casting, machining [79]–[81], while geometry constraints for additive manufacturing is beginning development [82]–[84].

Topology optimization manufacturing constraints for MBAAM would generate designs that offer minimum compliance while maintaining that there are not support structures, and thus self-supporting and compliant with the 15˚ rule, while also taking into account the bead thickness and width. Gaynor and Guest have implemented an overhang constraint, but these structures are not fully self-supporting due to how the algorithm includes intermediate densities [82]. Langelaar has developed an overhang constraint that uses a layer-by-layer approach to ensure self-supporting structures [85]. The technique assumes uniformly sized hexagonal elements, in which case the 45° overhang is used as the only option. For a different overhang angle, the aspect ratio has to be adjusted. Therefore, the overhang limit in MBAAM would need rectangular prism elements, which offer poor performance in finite element analysis. Brackett et al. have a technique for penalizing overhangs of certain lengths and angles based on heuristic techniques [86]. The topology optimization is completed, then the overhangs are identified through a linear regression analysis. The penalization function is subsequently added to the objective function and the optimization procedure continues. The use of manufacturing constraints for additive manufacturing is thus under-developed, and can benefit from more researchers working on the problem.

CHAPTER 3. METHODS

This chapter describes the design rules for MBAAM and their application to the excavator arm case study. The finite element analysis setup for the structural analysis of the printed arm is shown, and the application of topology optimization to generate the weight reduction holes is shown. The welding cell and equipment are then discussed.

3.1 Design Rules for MBAAM Geometry

The design rules for MBAAM are a result of the processing nature discussed in Chapter 2. The overhang constraint is a consequence of the weld bead behavior and torch orientation, which leads to the requirement of teardrop-shaped holes.

The print direction for the arm is decided on based on the expected cooling during welding. The vertical print direction is selected to keep the interpass temperatures high; as discussed in the background on heat flow in welding, the substrate temperature is an important factor in determining the quality of the deposited layer. By printing in the vertical direction instead of the horizontal direction, the interpass temperature of the layer will be higher, and thus thermal gradient and the associated residual stress and warping will be reduced.

3.1.1 Overhang Constraint

The overhang constraint in MBAAM is due to a combination of factors. The torch orientation is kept constant throughout there is no active control of build temperature. GMAW is usable in a variety of welding orientations, including overhead, in normal welding operation. However, MBAAM does not currently have orientation control

integrated into the slicing software. Additionally, there is no feedback control of the substrate temperature, so the likelihood of an overhang to overflow is significant. Thus, the printed arm geometry is compliant with the 15° overhang constraint. Inspecting the excavator arm geometry, the support plate circled in Figure 15 below violates the overhang constraint.
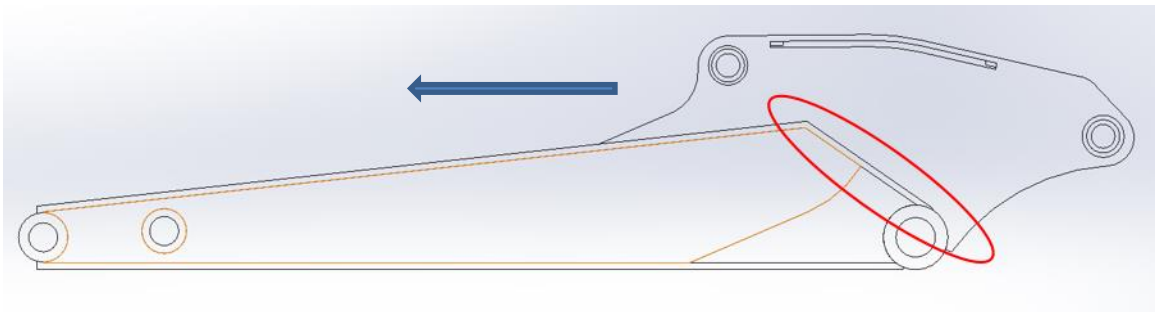
Figure 15. Arm plate geometry. The arrow shows the print direction and the circled section of the plate denotes an angle larger than 15° from the vertical direction.

3.1.2   Hole Geometry

The hole geometry is a direct consequence of the overhang constraint explained above. The holes for the lugs are thus in violation, and will be implemented in post processing. The holes from the results of the topology optimization are reinterpreted into teardrop shapes as in Figure 16 to reduce weight. Pilot holes, or holes with a smaller diameter than the desired hole that are subsequently drilled to proper size, for a mating surface cannot be printed unless the hole lies in the build plane, or the normal vector of the hole being parallel to the build direction.
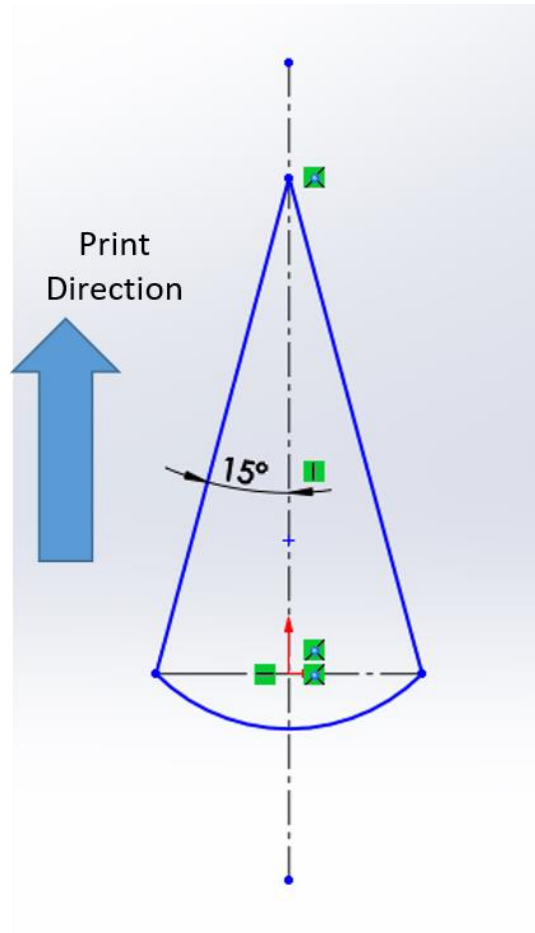
Figure 16. Example of a hole with MBAAM.

3.1.3 *Wall Thickness Relative to Bead Thickness*

The bead width in MBAAM is wide on the order of magnitude for plates used in structural applications. Beads are nominally 6mm +/-1mm wide and 2mm thick. If a structure is being designed for printing with MBAAM, the wall thicknesses are required to be multiples of the bead width. If an intermediate size is required, a post processing machining operation can remove material to the desired thickness. For instance, if a 14mm thick wall is needed, a three bead, or 18mm, thick wall is printed and the post processing machining removes 4mm.

In the case of the excavator arm, the original arm uses plates 8mm thick, while the MBAAM bead is 6mm wide. A CAD model with 12mm thick plates are used for the starting point of the topology optimization process to bring the overall weight to equal to the original. The final arm geometry uses thicknesses of 2 to 4 beads at different locations along the structure so assurance that the arm does not break in operation.

3.1.4   Modifying Features

The excavator arm has several features that must be modified prior to printing. Structural features can be modified to adhere to the design rules, and then the arm is checked with finite element analysis to ensure that the component will not fail under normal operating conditions. Mating surfaces are omitted from the printed geometry and implemented using a post processing machining operation.

The plate shown in Figure 15 is an example of a feature that needs to be modified, but is critical to the part's structural integrity. The modifications to make the plate compliant with the 15° overhang rule are checked via finite element analysis. Features that cannot be simply modified will use solid support structures for the printing process and then machined to the correct geometry in a post-process operation. The curved flange on the arm is an example of a feature that cannot be modified, since it is crucial for the range of motion of the arm. Figure 17 shows the flange outline form the original geometry. The bottom portion of the curve will be machined in post processing.
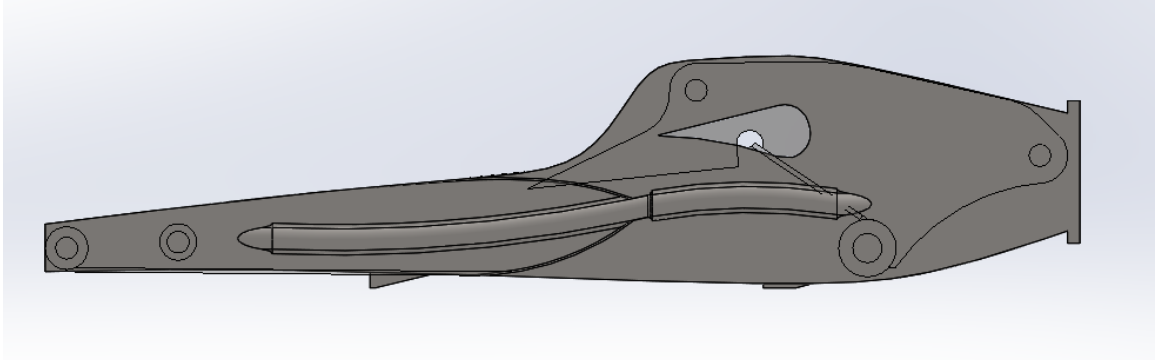
Figure 17. The flange outline is outlined over the as-printed geometry.

The pinned connections for the arm and boom and the hydraulic cylinders require pins and bushings with tolerances suited for load-bearing equipment. Thus, instead of printing a hole for the bearing sleeve, it is omitted from the printed part. The holes are instead machined during post processing, and standard bushings and bearing sleeves are welded in.

3.2 Modeling the Excavator Arm

This section presents the model of the excavator as developed in Abaqus. The load cases and finite element model setup are detailed.

3.2.1 Geometry

A schematic of a CNH Industrial CX55-B model excavator is shown below in Figure 18. The arm, boom, and bucket are labelled to avoid confusion; the name of the arm is different for different companies. The arm is 2.065m tall and weighs 133 kg.
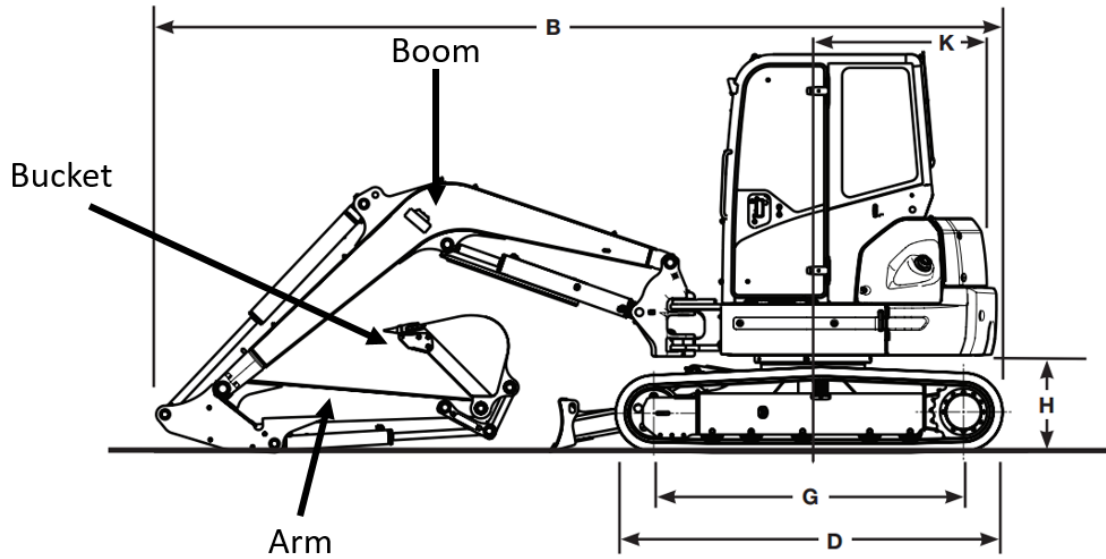
Figure 18. Adapted from the CX55B Specifications PDF.

3.2.2 *Load Cases*

The exact load values cannot be disclosed in this thesis, but the general force and moment vectors are shown for two load cases in Figure 19 and Figure 20 below. The load cases are for loads experienced in digging operation. The in-plane hydraulic loads are specified for a high cycle fatigue life. An allowable design stress of 250 MPa is used for the maximum allowable stress in the FE results of the in-plane loading.
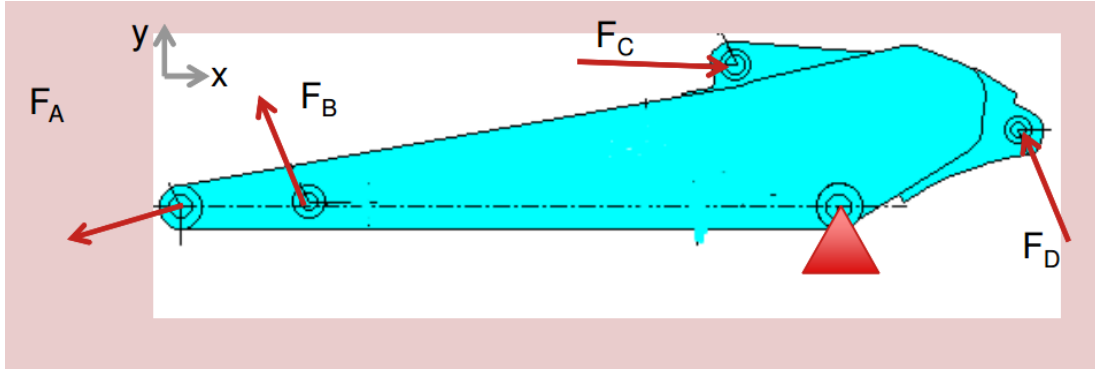
Figure 19. In-plane hydraulic loads from CNH.

A side and torsion load is also provided by CNH Industrial for a design load. Pin A in Figure 20 undergoes both a concentrated side load in the out-of-page direction and a torsional load with the normal direction going out of the page. The stress from the load must be kept under the yield stress of the metal. The model yield stress is 500 MPa.
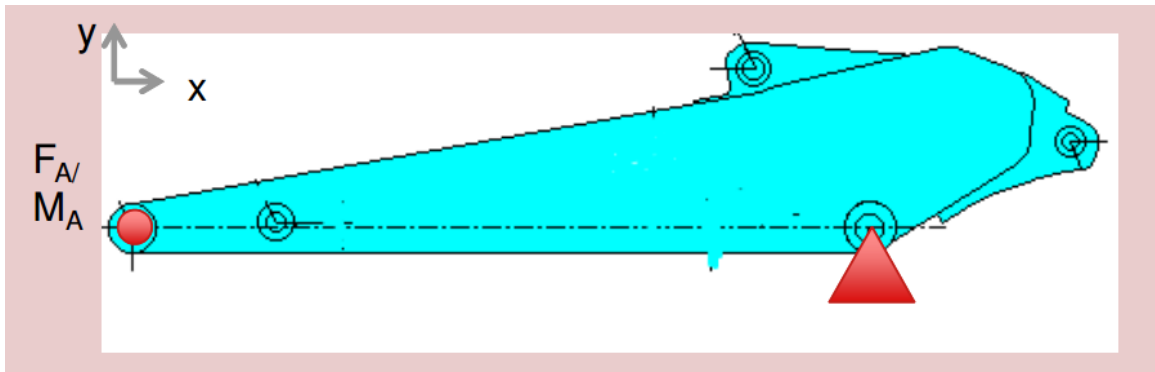
Figure 20. Side and torsion loads from CNH.

3.2.3   Finite Element Model Setup

The modified features on the excavator need to be checked via finite element analysis (FEA) to prevent the printed excavator from failing in the real world demonstration. The

39

original arm geometry is analyzed for baseline comparisons, and all subsequent versions of the arm geometry are analyzed using the same FE setup.

The CAD file is exported to Abaqus as an ACIS file. The elastic properties of a generic carbon steel are listed below in Table 2. The maximum stress in the arm must be less than the yield stress of generic steel, so only the elastic properties are needed.

Table 2. Carbon Steel Properties for FE Model

	Elastic Modulus	Poisson's Ratio	Density
Carbon steel	210 GPa	0.3	7850 kg/m^3

The imported geometry is meshed with quadratic tetrahedral elements with a nominal element size of 1cm. Tetrahedral elements are used because the curved geometry of the arm is difficult to mesh using hexahedral elements. This generates 300,000 to 400,000 elements with over one million degrees of freedom.

The loads are applied using a multiple point constraint feature in Abaqus. The inside surfaces of the lugs are constrained to follow the rectilinear displacement of a reference point at the center of each lug, but rotational displacement is not constrained. This leaves the pins to act as true pinned connections and the applied force is evenly distributed across the mating surfaces.

3.2.4 FE Model of Stock Geometry

The finite element analysis results for the stock geometry are interpreted to learn how to design the final arm geometry, since the final arm geometry is to withstand operation at the original specifications.

The prescribed in-plane loads from the hydraulic cylinders are compressive at the flanges and tensile at the bucket pin. The side view in Figure 21 shows that the side of the excavator is close to being the central axis. A common rule in fatigue life for soft steel is to use half the ultimate strength as the stress at which the component can endure unlimited cycles without failure. The CNH requirements are for the arm to undergo over high cycle fatigue under this load, so the assumption of 50% of the monotonic yield strength (the yield strength is modeled as 500 MPa) as the maximum allowable stress is a conservative estimate.
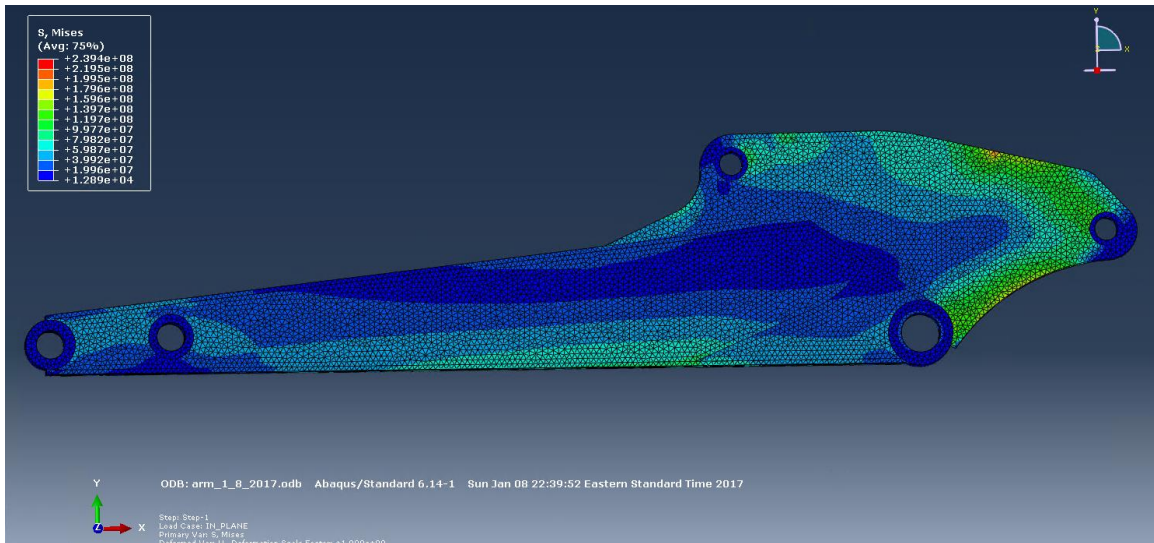
Figure 21. Side view of in-plane hydraulic loads on stock geometry.

The stress concentrations shown in Figure 22 are due to the compressive stresses from the bucket and arm cylinder being extended to simulate digging. The reaction forces from the

41

extending cylinders puts the thin wall flanges in compression. The walls are thin enough

to be at risk for buckling, and the geometry sets up stress concentrations.
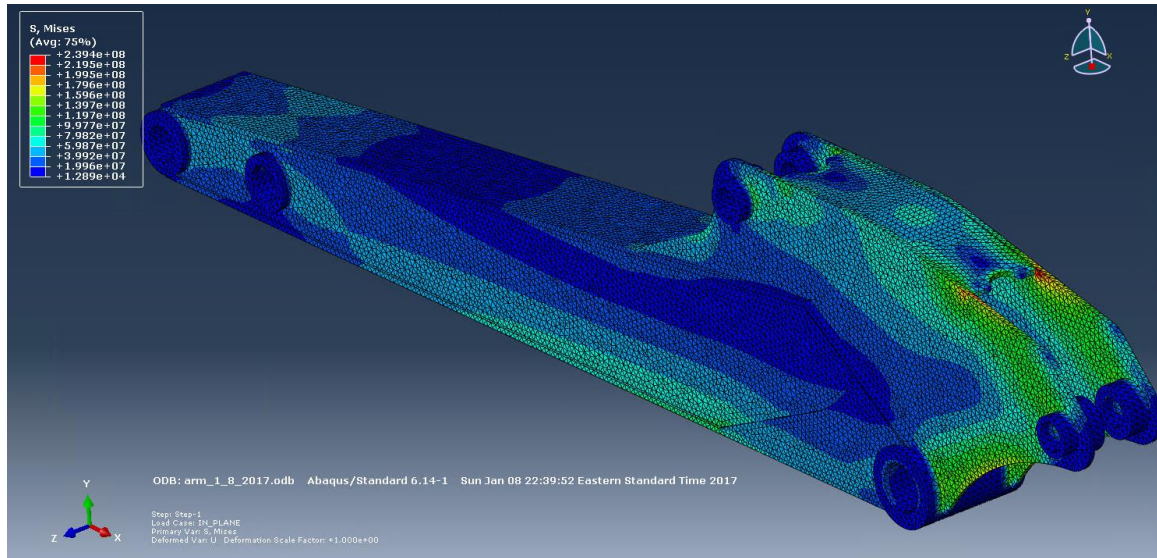
Figure 22. Stress concentrations at top flange show effects of compressive stress on a thin wall mated to a support.

The side and torsion loading is now considered. The requirements for this load case is to

not damage the arm under loading. The FE results show an acceptable stress of 239 MPa

at the stress concentrations which satisfies our self-imposed safety factor of 250 MPa.

The stress from the bending load is transferred to the box structure. The plate welded to

the pinned lug prevents a compressive stress that would cause failure. The neutral axis of

this bending box structure, seen as the blue section on the box structure in Figure 23 follows

elementary beam theory.
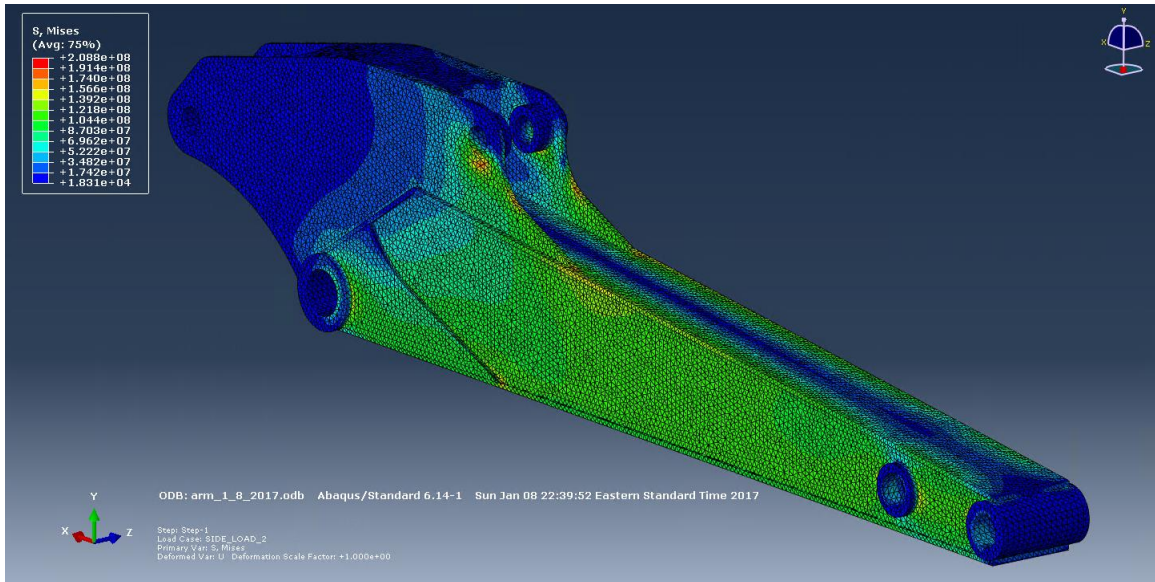
Figure 23. Side view. Stress concentrations around the top lug and the neutral axis are expected.

Figure 24 shows a cutaway view of the stress imposed by the side loads. The lugs are not highly stressed (< 18 kPa) except for where they join with the box structure. This corresponds to how the lug sleeves are welded to the plates, and makes for a more accurate model.
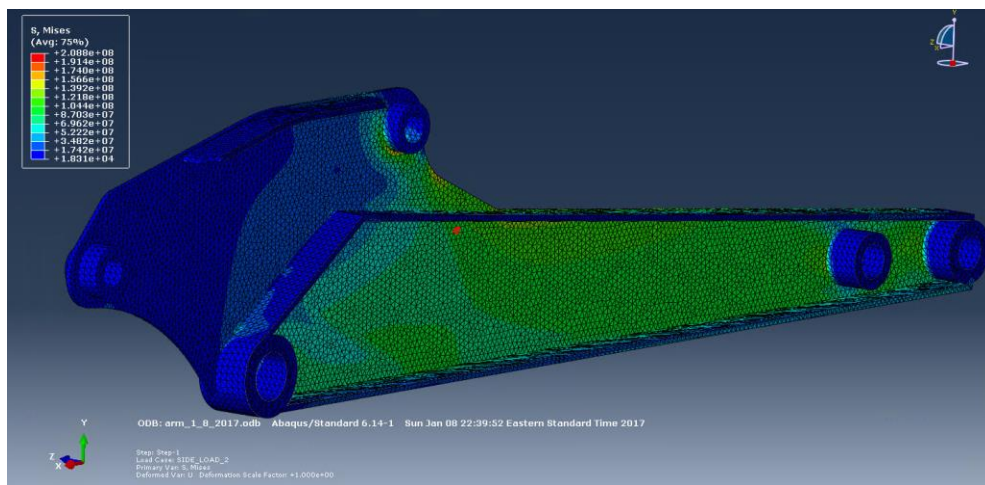
Figure 24. Inside cutaway of side load.

3.3   Topology Optimization for MBAAM

Since MBAAM wall thicknesses are in multiples of 6mm while the excavator arm uses welded 8mm thick plates, the printed arm will use topology optimization to print 12mm thick walls with holes optimally placed to reduce the weight of the arm. Manufacturing constraints for MBAAM are not available for topology optimization, so the results will be reinterpreted using the design rules previously discussed. The topology optimization is performed using Abaqus's built-in TOSCA package.

Topology optimization minimizes an objective function subject to one or more constraints in a domain known as the design space. Given that the objective function is the compliance of a structure, the design space is thus the part of the structure that is to be optimized. In the case of the excavator arm, the design space is the entire arm, excluding the pinned joints and their immediate surroundings. The edges of the design space is the outline of the excavator arm, which needs to be maintained for the kinematics and range of motion of the assembly. Thus, the design space is the full volumetric envelope of the arm. Filling the entire design space, meaning the elements considered for optimization, with solid material increases the computational requirements. The resulting geometry is also generally not printable with MBAAM.

The user can use intuition to sculpt the design space from the most general to a more feasible starting place, thus the topology optimization algorithm can find the minimum of the objective function more quickly. Aremu et al. [87] suggests that while starting with a simpler starting geometry reduces computational time, the "optimal" results are a local minimum, not the global minimum, for the design space. However, if a lower local

minimum or global minimum exists, it will likely be outside of the manufacturing constraints and thus infeasible.

Other additive manufacturing processes can take advantage of maximizing the design space since the manufacturing constraints are relaxed by use of support structures, but the applicability of topology optimization to MBAAM suggests that the starting point for the optimization be sculpted. For example, if a solid excavator arm were to be used as the starting point for optimization, the results would not be able printable using the current design rules. The starting point for the excavator arm is thus restricted to that of a thin wall geometry to determine where holes should be placed.

Using the Abaqus FE and TOSCA setup described in Chapter 3, a model with 12mm thick walls to correspond to 2 bead thick walls deposited using MBAAM is used with the minimum compliance algorithm. The volume constraint is set as 70% of the original volume, and the lugs are not included in the design space. The setup is summarized in Table 3 and the CAD model used is shown in Figure 25. Volume is preferred to mass in multi-material optimization [88] and truss cross section optimization, and is only used in topology optimization for familiarity. Volume is proportional to mass via density, so the effective results are identical.

Table 3. Setup of optimization algorithm.

Design variables	Strain energy, volume
Objective function	Minimize strain energy over all load cases
Constraint	70% of the original volume
Geometry restriction	Lugs are not considered in the design space
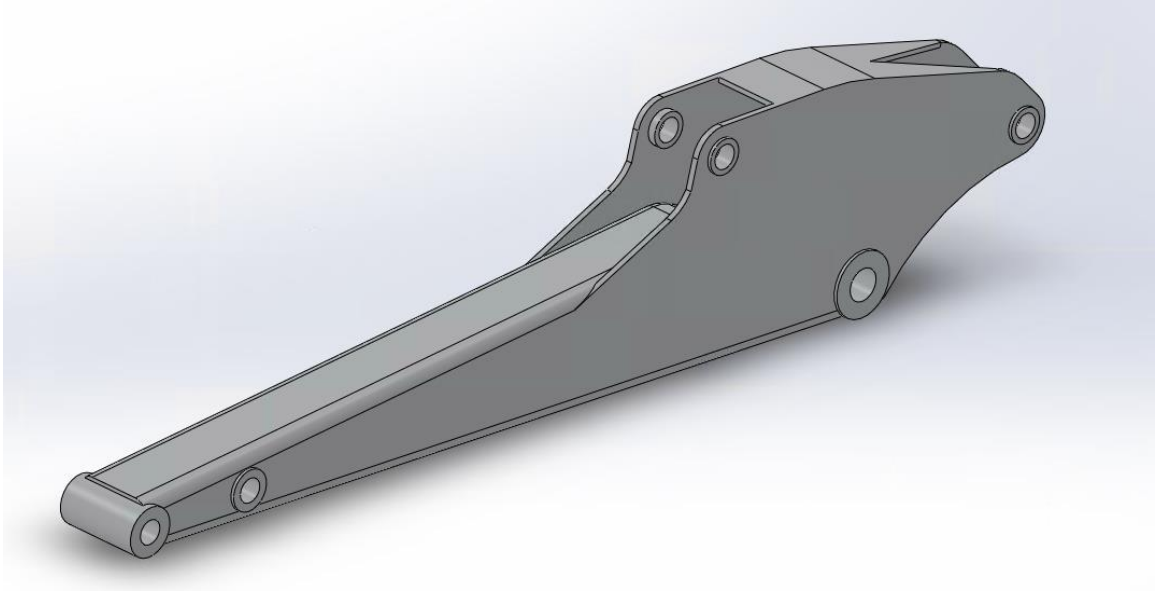
Figure 25. Starting geometry for topology optimization.

Internal hydraulic lines are included in the topology optimization to consider the added stiffness of the proposed hydraulic lines. These lines are shown in Figure 26. This geometry is different from the stock geometry by blending the flanges and rounding the corners of the box structure. Rounded corners are not possible with the standard welded arm; bending stress will be reduced as a result.
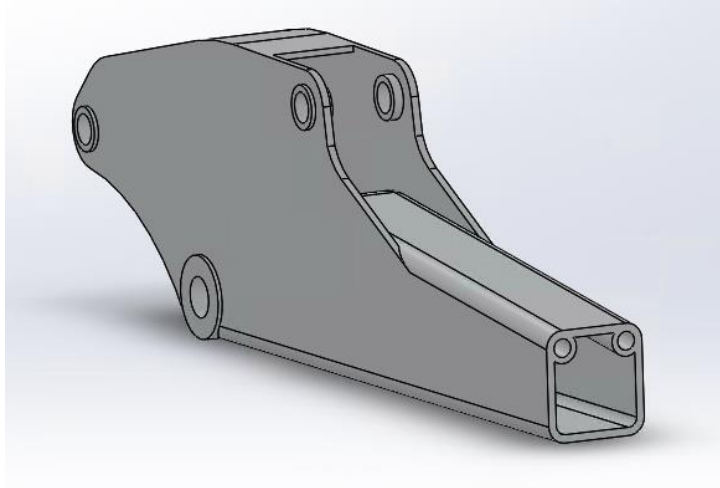
Figure 26. Cutaway of starting geometry for topology optimization.

The results of the optimization are shown in Figure 27. This geometry has used a built-in smoothing algorithm in Abaqus to reduce the jagged edges inherent in the removal of elements. Increasing the number of elements helps to smooth the surface, but the computational expense increases too much to be usable.
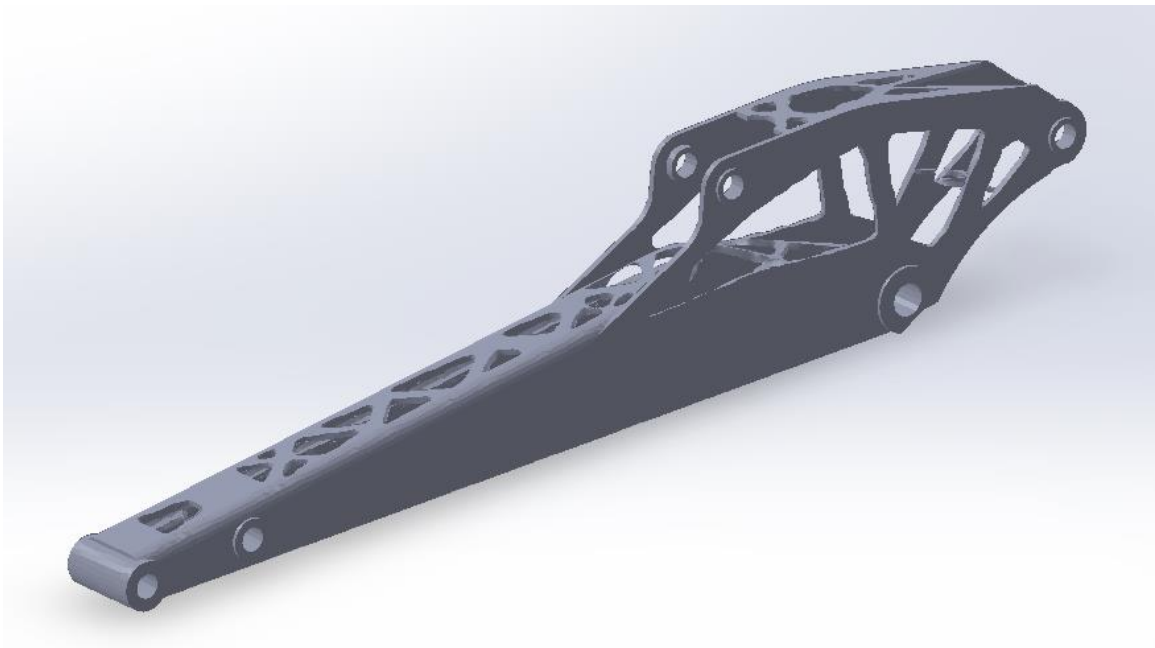
Figure 27. Surface smoothed output of SIMP algorithm.

Qualitatively, TOSCA takes much of the top and bottom of the box structure off, while leaving the sides. The flanges are also mostly not needed, but the proposed geometry is not printable with the current manufacturing constraints. Figure 28 below shows how the SIMP algorithm within the TOSCA package has penalized the top and bottom of the box structure and the flanges. The plot shows the normalized, or relative, element densities. SIMP had penalized the elements with relative densities less than 1. The filter removes any element with a relative density less than 0.3.
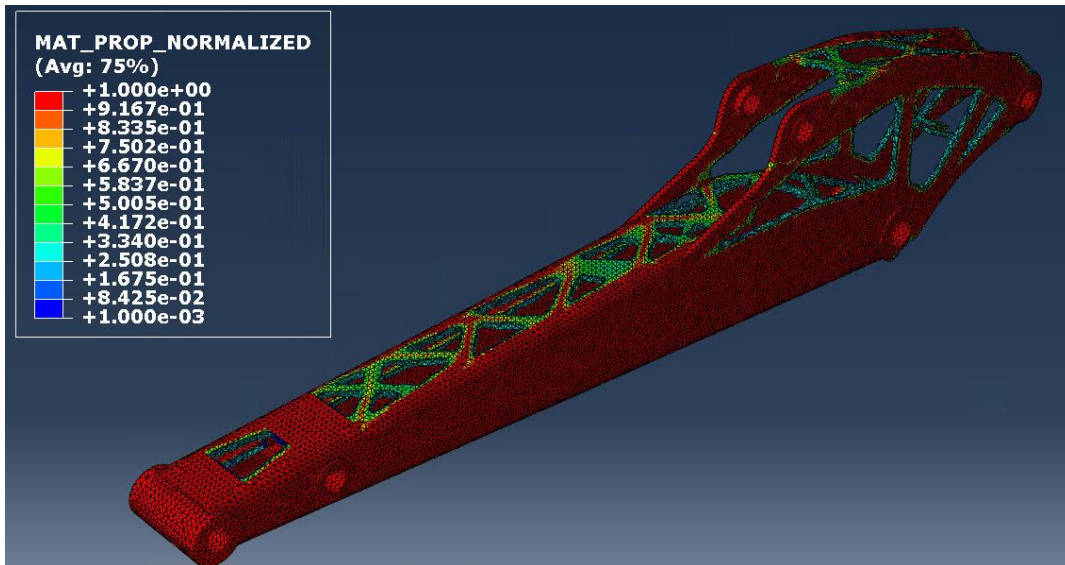
Figure 28. Relative element density. Red is 1, blue is 0.

The weight of the standard excavator arm is 129kg, while the 12mm thick wall model with hydraulic channels is 166kg. The 70% volume constraint described earlier is used to bring the optimized excavator's weight to approximately 120kg. The result of the topology optimization is a fictitious structure that has effectively different materials where elements have different densities, as previously shown in Figure 28 and explained in the section on

topology optimization in Appendix A. The optimized geometry is considered in the final arm geometry, since the recommended holes are not possible to print.

The low pass element density filter demonstrates the importance of the penalization factor p in the SIMP formulation. Clearly, when $\rho = 0$, the element is a void and when $\rho = 1$ the element has its normal properties, although in this project the minimum relative density is set to be 0.001. The penalization factor pushes the elements with intermediate densities to become voids. The recommended values of p for three dimensional problems are 3 or higher, although the numerical instabilities discussed in the background section can show when the p value is too high.

A flowchart of how TOSCA iterates through a structural optimization problem is shown in Figure 29. The default number of iterations provided for convergence is 50; if the number of iterations exceeds 50, the operation will stop and the optimization procedure must be restarted using a higher number of available iterations. This thesis uses convergence criteria of less than 0.001 unit change in the objective function and 0.005 unit change in the element density. Both of these criteria must be met for TOSCA to converge. The message file of the results is automatically generated and can be checked for convergence.
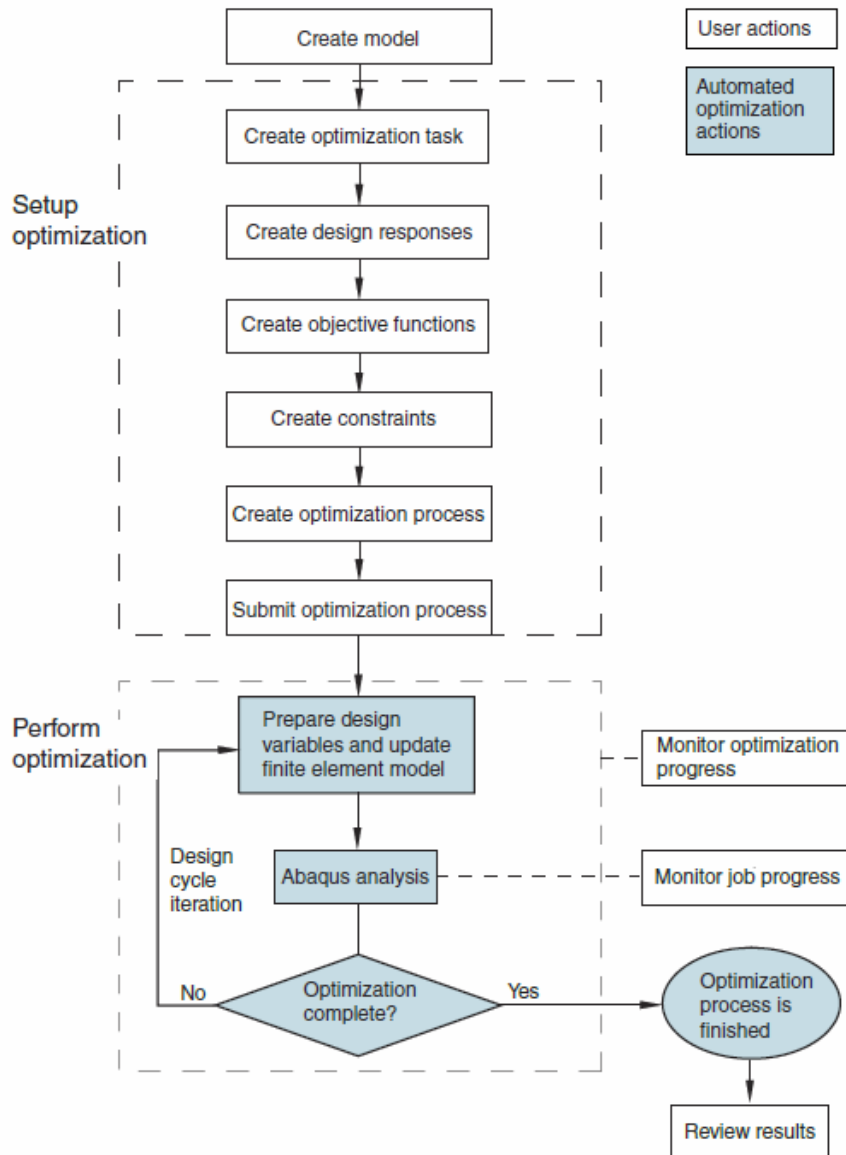
Figure 29. Flowchart from Abaqus documentation on the topology optimization procedure.

3.4   Welding Cell and Equipment

The Oak Ridge National Laboratory (ORNL) and Wolf Robotics have collaborated to

modify Wolf's Wolfpack product line for the MBAAM. Custom modifications for loading

the path trajectories into the system from the ORNL slicer have been implemented by ORNL and Wolf.

The excavator arm was printed in a modified Wolf welding cell. The GMAW power source is a Lincoln Electric Power Wave R500 Robotic Power Source and Surface Tension Transfer modular unit, both shown in Figure 30 .

Figure 30. Lincoln Electric R500 Robotic Power Source with Surface Tension Transfer module [89]**.**

Figure 31 below shows the inside of the welding cell with the ABB 6 DoF manipulator arm. The wire feeder attached to the ABB manipulator has three rollers in series to straighten the incoming wire and prevent it from missing the melt pool due to pre-set curve in the wire.

Figure 31. Wolf Robotics Wolfpack cell.

CHAPTER 4. RESULTS AND DISCUSSION

The arm geometry that follows MBAAM design rules is presented. The as-printed geometry is then machined to result in the arm that is installed on the excavator. An FE model of the final geometry is compared to the original to show that the new arm geometry is designed to the same specifications as the original. A discussion on how the manufacturing constraints have affected the geometry follows.

4.1   Final Arm Geometry

The culmination of design rules, finite element analysis of the stock geometry, and topology optimization are used to generate the final arm geometry. A CAD model of the as-printed arm geometry is shown below in Figure 32. The flanges are extended to obey the 15° overhang limit.
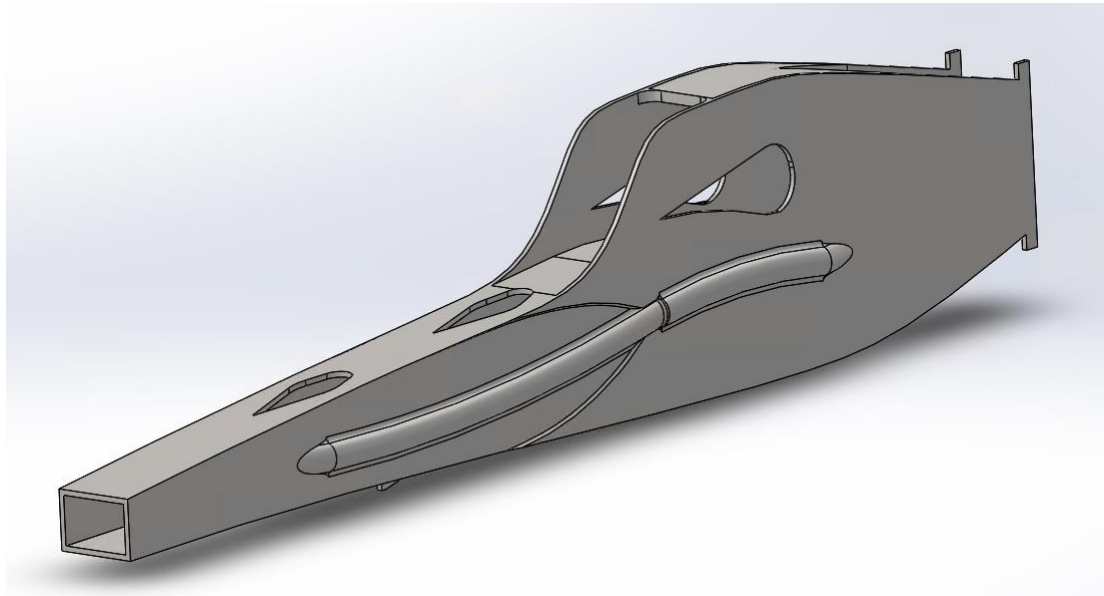
Figure 32. As-printed arm geometry. The holes for bearing sleeves and the curves for range of motion are omitted.

The as-printed geometry is shown from the side in Figure 33. The fins on the bottom are for the machine shop operators to align the part in the CNC machine. The machining operation cuts the holes for the bearing sleeves and the flanges are contoured to the desired curvature.
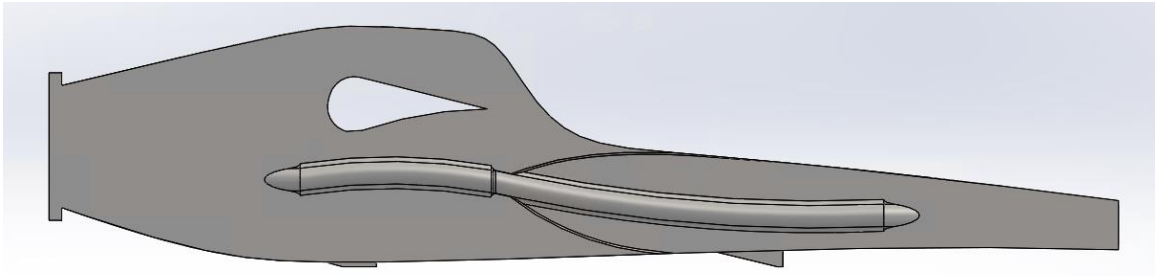
Figure 33. Side view of the as-printed arm geometry.

Figure 34 shows a CAD model of the printed arm after post-processing. The internal hydraulic lines used for the topology optimization (shown in Figure 26) are moved to protrude out from the sides of the box section to demonstrate the integrated lines. These hydraulic lines are not currently functional, although they could be used to connect to auxiliary equipment such as a movable thumb, rotational gimbal, or hydraulic hammer.
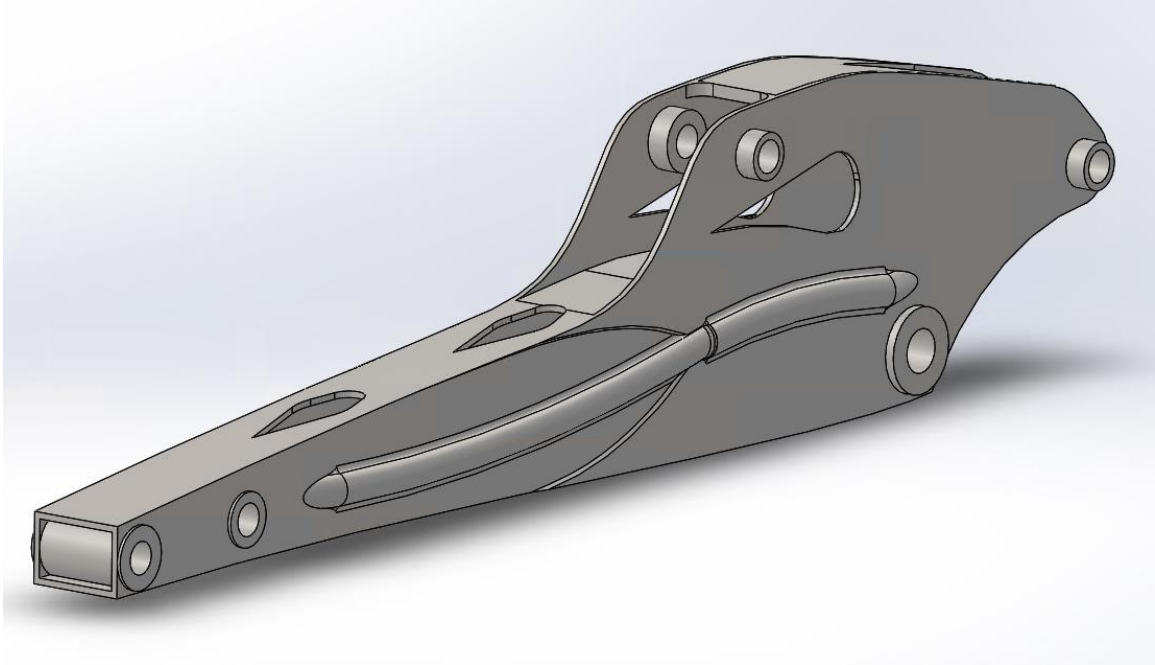
Figure 34. Final arm geometry.

4.2   Finite Element Analysis Results of Arm Design

The feasibility of using MBAAM to make functional replacements requires that the new components be comparable in mechanical performance. The changes made for the final arm geometry are checked via finite element analysis for stress overloads.

4.2.1   In-Plane Hydraulic Cylinder Loads

The load cases provided by CNH are used as benchmarks for the new arm geometry. The hydraulic cylinder loads are applied to the geometry, the results of which are shown in Figure 35. The maximum stress of 290 MPa is located at the flange support, which is a stress singularity: the stress concentration seen there does not stop increasing with smaller mesh sizes. The average stress values along the box structure are varies between 15 and 45 MPa, and the flange undergoes stresses between 140 and 160 MPa. These compare well to

the stock geometry, shown in the previous chapter in Figure 21. The average stress in the box structure is lower for the final arm geometry. The stress concentration at the flange support, shown in Figure 36, is a stress singularity.
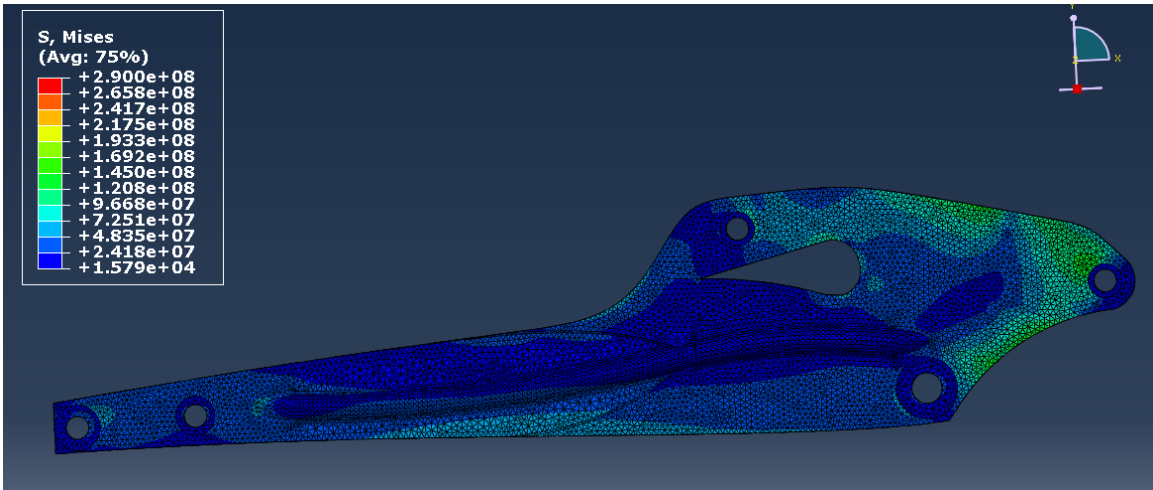
Figure 35. In plane hydraulic cylinder loading on ORNL optimized geometry.
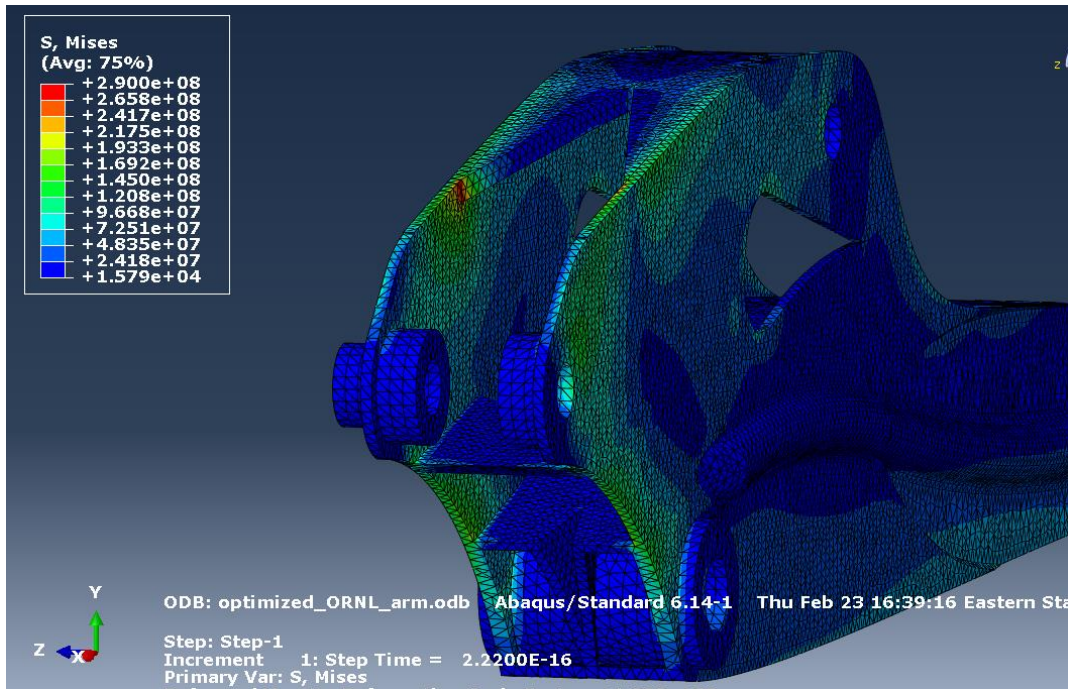
Figure 36. Rear view of ORNL optimized geometry.

The teardrop shape holes undergo a stress distribution similar to that expected for the elementary elastic analysis of a hole in a plate under axial load. The stress around the holes are seen in Figure 37, but the stresses are low enough to not be a concern.
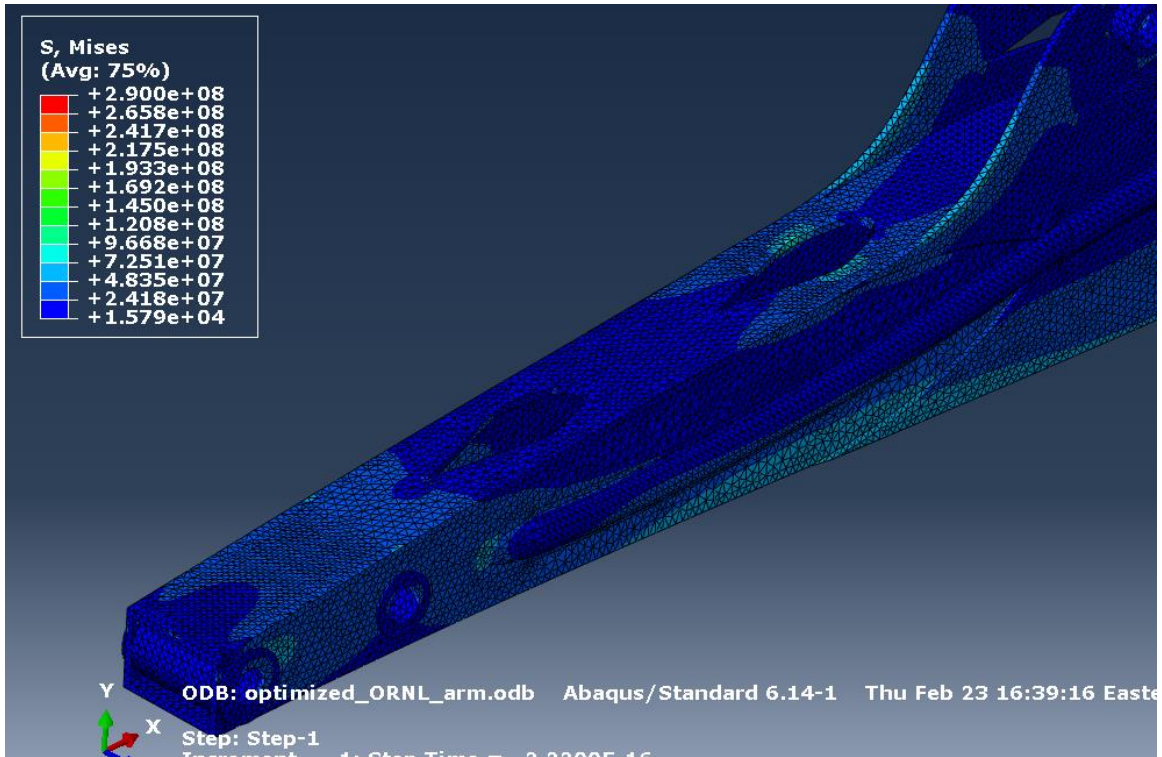
Figure 37. Top view of ORNL optimized geometry.

4.2.2   Side and Torsion Loads

The side and torsion loads provided by CNH are now applied to the final arm geometry. The stress distribution is shown in Figure 38Figure 44. The box structure undergoes the majority of the stress, as expected from the results of the stock printable, and optimized arms. The stress concentration is found where the hydraulic fluid line ends and merges with the box structure. This is again a stress singularity, and is not expected to be an issue in operation.
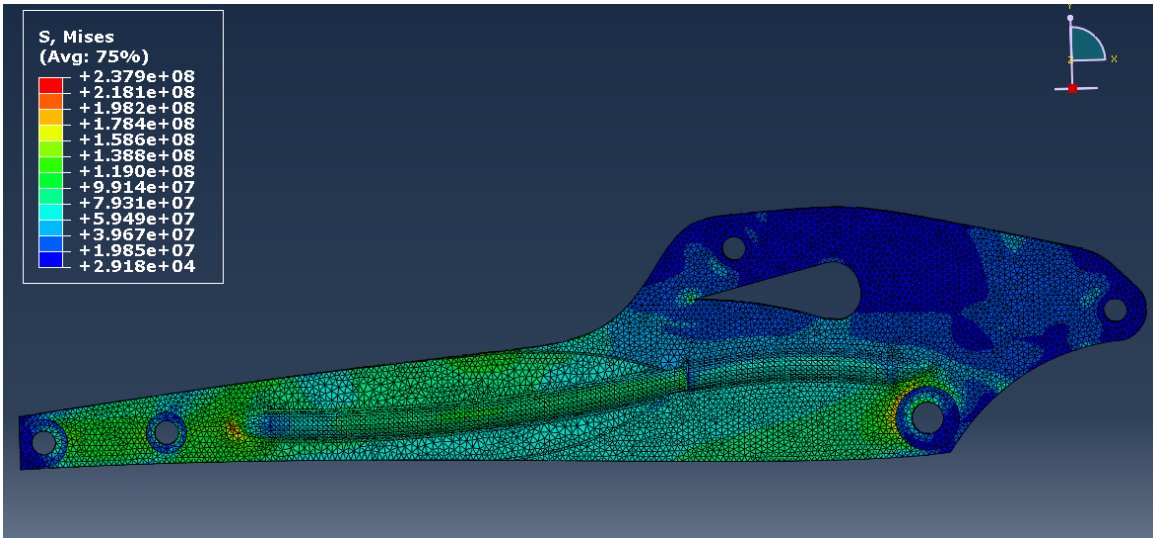
Figure 38. ORNL geometry side load

A top view of the stress distribution due to the side and torsion loads is shown in Figure 39. The holes on the top of the box structure undergo a stress concentration where the holes are bridged.
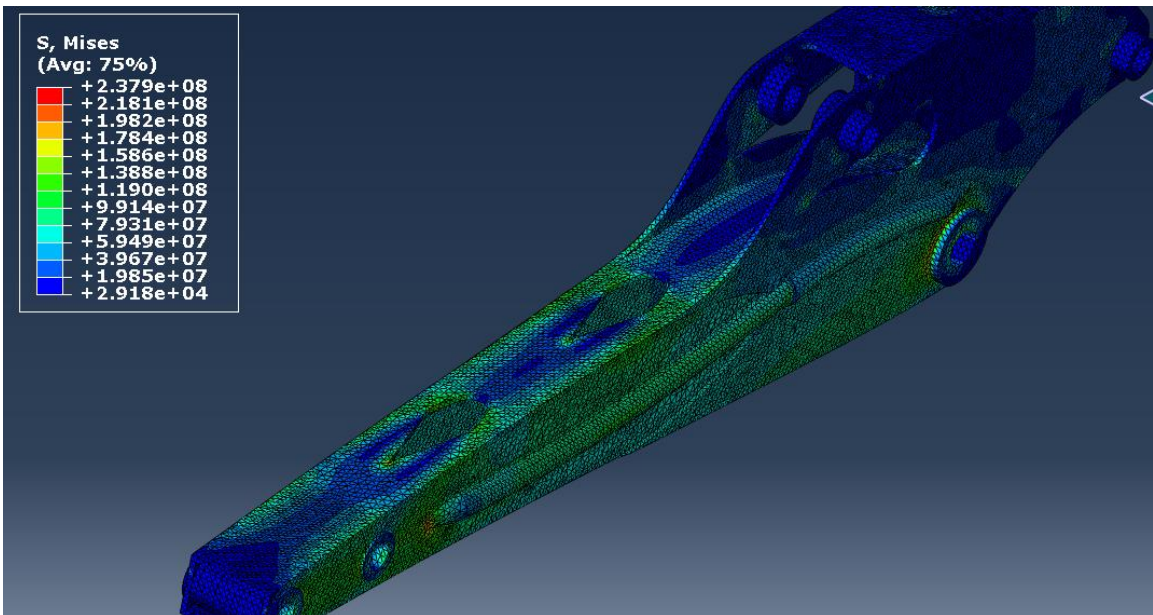
Figure 39. Side loading on ORNL geometry.

4.3   Completed and Installed Arm

The full arm was printed in late January 2017. This section discusses the process from printing to post-processing to assembly on the excavator. The replacement arm proved to be a success and successfully replaced the existing stock arm.

Investigation into the difference between the CAD model and printed part shows that in the print direction (vertical axis), the dimensional error is +/- 0.50mm. The total length of wire exceeded 13 miles (21km) and the time to print was over 5 days of continuous operation. Figure 40 shows the arm after printing but while still clamped to the plate. The plate is bolted to the floor rather than the included rotary table so that the visible weld gun can use its full work envelope.

Figure 40. The full arm after printing.

The four holes in the arm were based on the suggestion of the topology optimization. The quality of the as-printed holes is shown in Figure 41. The molten weld metal had some overflow, but this is expected when building on an overhang. The surface could be finished during post-processing, but the holes are not currently finished.

Figure 41. Cut-out hole in printed arm.

The integrated hydraulic line are shown in detail in Figure 42. The hydraulic lines are for demonstration; they were originally hidden inside the structure, but having them protrude from the side highlights the use of functional structures.

Figure 42. Support plate and hydraulic line close up.

The completed arm is sent to ORNL's in-house machine shop to develop the protocols for finishing the surface, cutting holes for mating surfaces, and bringing the flange curves to tolerance. The bearing sleeves are welded in using ER70S-6 wire. Figure 43 shows the surface of a test article after machining. The installed arm's surface is not finished to demonstrate the expected surface finish after printing. If an arm is intended use the printed arm for everyday operation, the surface should be finished to help prevent fatigue crack formation.

Figure 43. Test section of the arm to demonstrate finished surfacing and welding of the bearing sleeves.

Figure 44 shows a side view to better see the welded sleeves and lugs installed. The cylinders will be attached via a ground pin in these lugs. The image also shows the bottom side of the arm which has not been machined. A clear coat has been applied to prevent the surface from rusting while still showing the surface finish. The final arm geometry does not use a clear coat, but a silver paint job instead.

Figure 44. Alternative view of the machined arm and the welded-in sleeves.

The installed arm is shown in Figure 45. As mentioned before, the surface of the arm is not finished to show the as-printed condition. Silver paint is also applied for aesthetics. The holes have slots cut to prevent stress concentrations, which was not done in conjunction with this thesis, but is mentioned here to explain the difference in appearance. The arm was used to dig holes in sand, and proceeded with no issues with the arm.

Figure 45. The arm installed on an excavator [90]**.**

CHAPTER 5. CONCLUSIONS AND CONTRIBUTIONS

MBAAM is a new metal additive manufacturing process that surpasses the build volumes and rates of other metal AM processes. However, the increased deposition rate results in low resolution. The overhang constraint of 15° and lack of support structures complicate the design process for replacement structural components, but through structural analysis, the new structure can be rated to the original specifications. The overhang constraint is due to the lack of automatic tool orientation control and the potential for the melt pool to flow over the side of the thin walls. Solid support structures can be used if absolutely necessary, but the supports are full strength steel and need to be machined in a post process operation. The design rules for MBAAM can be concisely expressed as:

1. An overhang limit of 15°.

2. Lack of easily-removable support structures.

3. Features are deposited in multiples of the nominal bead width.

If a wall is designed to be 14mm thick and the nominal bead thickness is 6mm, then the final part will have to be printed at 18mm thick walls and then post processed to bring the thickness to the specified dimension. The other option is to redesign the part to be 12mm thick and add reinforcement measures as required by the stress analysis. If the wall has an overhanging feature, it will not print unless the overhang is less than 15° with respect to the print direction. If the feature exceeds the limit, the part must either be redesigned or solid supports implemented and then removed in a post processing machining operation.

The excavator case study demonstrated how the design rules for MBAAM are applied to large structural components. The features of the excavator were grouped into feasible and infeasible geometry, with the infeasible geometry implemented in post processing. The feasible geometry included the section of the arm's box structure that violated the 15° overhang constraint but could not be post processed (*e.g.* machined) to the exact tolerance after printing since surfaces to be machined are not accessible. This feature was instead elongated to meet the 15° overhang requirement.

The flange outlines and holes for the bearing sleeves were classified as infeasible due to the overhang constraint, and were omitted from the printed geometry. These features became solid support structures to permit printing of the material above them, and a post processing milling operation then implemented the outlines and holes. Holes to reduce weight were included in the printed geometry, although the shape of the holes were adjusted to "teardrop" shapes following the 15° constraint (as in Figure 16) to close the geometry.

The printed arm had a 33% weight increase over the stock arm: the weighs 172 kg and the stock arm weights 129kg. The geometrical accuracy exceeded expectations, with a print-direction, or z-direction, tolerance of 0.5mm achieved over the 2 meter arm. These results showed that MBAAM can produce geometries within dimensional specifications, highlighting its utility for replacement components.

The approximate deposition rate of 600 cm^3/hr permitted the excavator arm to be printed in 5 days. The build volume is on the order of 10,000 cm^3 using the current robot arm, but can be easily extended using a robot with a larger work envelope. Future efforts to design

and print structural components will benefit from experience with the requirements, so that spending a week to design the part, a week to print that part and then another week for post processing will result in a custom-made structural component. The lessons learned from designing and building this excavator arm have illustrated some recommendations for future projects; these are described in Chapter 6.

CHAPTER 6. RECOMMENDATIONS

Several recommendations can be made to bring more flexibility and reliability to MBAAM as a manufacturing process. Addressing the overhang constraint, post processing requirements, and deposition rate is key to reaching these goals.

1. **Overhang constraint**. The MBAAM design rules limit the overhang to 15° or less; this dramatically restricts the feasible geometry. It is recommended to utilize a path planning tool to change the tool and table orientations. This would increase the overhang limit by reducing the chances of the weld bead overflowing when building on an incline.

2. **Hybrid arc weld deposition and CNC machining**. Incorporating a milling head into the MBAAM process would decrease time and potential for operator errors by eliminating the need to re-fixture the part later in a machine shop. Inner surfaces could also be machined to a smooth finish, rather than leaving the as-deposited weld beads.

3. **Increasing deposition rate**. GMA welding has a limit to deposition rate, since defects such as humped beads form when welding too fast. Adding a second heat source such as a GTAW power source or laser will increase the maximum deposition rate.

4. **Decrease topology optimization computation time**. The topology optimization strategy used to generate the cutout holes in the structure takes upwards of 8 hours on a high end workstation. It is recommended to use a computing cluster with more computing cores on a scalable system.

5. **Manufacturing constraints for additive manufacturing in topology optimization**. Topology optimization can reduce the chances for infeasible geometry to be generated through constraints. To date, little progress has been made in developing additive manufacturing-specific constraints for topology optimization. Having an overhang constraint would reduce the amount of time needed to re-interpret the topology optimization results for printing.

6. **Repeatability and reproducibility**. As MBAAM is used for more applications, the need to understand issues with repeatability and reproducibility of bead geometry increases. This will provide confidence that the alignment on a pin joint, for example, will not cause interference problems during operation.

These recommendations are the most pressing for improving the flexibility of MBAAM as a manufacturing process. Further recommendations include thermal management to maintain a constant inter-pass substrate temperature. A combination of thermal modeling and imaging techniques can solve this problem for future studies.

APPENDIX A. METHOD OF MOVING ASYMPTOTES

DERIVATION

The goal of topology optimization is to determine the material distribution that minimizes the structure's compliance at the specified volume constraint. This appendix derives the topology optimization algorithm used by TOSCA. The algorithm is a combination of the Method of Moving Asymptotes and Solid Isotropic Material Penalization methods to arrive at a fictitious structure for design concept generation.

The arm is assumed to always be elastic, which is reasonable given that no plastic deformation should occur during normal operation of the excavator arm. This derivation follows Bendsøe and Sigmund [91] and Svanberg [64].

Structural problems use the following elastic variational formation. The three dimensional structure to be optimized is assigned a domain Ω^m, a subset of the reference domain Ω. Using the principle of virtual work, we define the minimization problem over admissible displacement fields.

$$\min_{u \in U, \Theta} \int_\Omega fu\mathrm{d}\Omega + \int_{\Gamma_T} tu\mathrm{d}s \qquad (4.)$$

Subject to:

$$\int_\Omega E_{ijkl}(x)\epsilon_{ij}(u)\epsilon_{kl}(v)\mathrm{d}\Omega = \int_\Omega fv\mathrm{d}\Omega + \int_{\Gamma_T} tv\mathrm{d}s \qquad (5.)$$

for all $v \in U$

$$C_{ijkl}(x) = \rho(x)C^0_{ijkl}$$

$$Vol(\Omega^m) = \int_\Omega \rho(x)\mathrm{d}\Omega \leq \mathrm{V} \tag{6.}$$

$$0 \leq \rho(x) \leq 1, \qquad x \in \Omega$$

This is the weak variational form of the elasticity problem inserted into the optimization problem. E_{ijkl} is the elastic tensor (assumed isotropic), x are the finite elements, ε_{ij} and ε_{kl} are the strains for the deformed and un-deformed states, respectively. U is the space of kinematically admissible displacement fields, u is the equilibrium displacement, f is the body force vector, t is the boundary traction vector. The coefficient $\rho(\mathrm{x})$ acts as the density of the material, scaling the stiffness of the point x. The coefficient is defined later in the descretized formulation of the compliance minimization problem. The volume constraint $Vol(\Omega^m) \leq V$ sets the total volume of the domain Ω^m to be equal to or less than a specified volume V.

The elastic variational formula of the minimum compliance stated above is now discretized for use in finite element analysis. The minimization problem becomes

$$\min_{\mathbf{u},E_e} \ \mathbf{f}^T\mathbf{u} \tag{7.}$$

Where $\mathbf{f}$ is the load vector and $\mathbf{u}$ is the displacement vector.

$$\mathrm{s.\,t.:} \ \mathbf{K}(E_e)\mathbf{u} = \mathbf{f}, \qquad E_e \in E_{ad} \tag{8.}$$

and $\mathbf{K}$ can be written as

$$\mathbf{K} = \sum_{e=1}^{N} \mathbf{K}_e(E_e) \tag{9.}$$

where $\mathbf{K}_e$ is the global element stiffness matrix. This discretized formulation is used hereafter.

A sensitivity analysis of each element at each iteration is needed for the updating scheme. The sensitivity of an element is the derivative of the compliance function $c(\rho_e)$ with respect to ρ_e. This gauges how sensitive the compliance is to changes in density. The results are used to rewrite the optimization problem as a convex subproblem in the Method of Moving Asymptotes formulation.

$$\min_{\rho_e} c(\rho_e)$$

$$\text{s.t.} \sum_{e=1}^{N} v_e \rho_e \leq V \tag{10.}$$

$$0 \leq \rho_{min} \leq \rho_e \leq 1, \qquad e = 1, \dots, N$$

The function $c(\rho) = \mathbf{f}^T\mathbf{u}$ and $\mathbf{u}$ solves $\sum_{e=1}^{N} \rho_e^p \mathbf{K}_e \mathbf{u} = \mathbf{f}$. The objective function $c(\rho)$ adds the zero function

$$c(\rho) = \mathbf{f}^T\mathbf{u} - \bar{\mathbf{u}}^T(\mathbf{Ku} - \mathbf{f}) \tag{11.}$$

where $\bar{\mathbf{u}}$ is a fixed arbitrary vector. The sensitivity of the objective function with respect to density is

$$\frac{\partial c}{\partial \rho_e} = (\mathbf{f}^T - \bar{\mathbf{u}}^T \mathbf{K})\frac{\partial \mathbf{u}}{\partial \rho_e} - \bar{\mathbf{u}}^T \frac{\partial \mathbf{K}}{\partial \rho_e} \mathbf{u} \tag{12.}$$

When $\bar{\mathbf{u}}$ satisfies the adjoint equation $\mathbf{f}^T - \bar{\mathbf{u}}^T \mathbf{K} = 0$, the sensitivity simplifies to

$$\frac{\partial c}{\partial \rho_e} = -\bar{\mathbf{u}}^T \frac{\partial \mathbf{K}}{\partial \rho_e} \mathbf{u} \tag{13.}$$

This result also shows that $\bar{\mathbf{u}} = \mathbf{u}$. From earlier, the compliance sensitivity can be rewritten

as

$$\frac{\partial c}{\partial \rho_e} = -p\rho_e^{p-1}\bar{\mathbf{u}}^T \mathbf{K}_e \mathbf{u} \tag{14.}$$

The objective function can be approximated using the Method of Moving Asymptotes. Approximating around a point,

$$c(\rho) \approx c(\rho^0) + \sum_{e=1}^{N} \left(\frac{r_e}{U_e - \rho_e} + \frac{s_e}{\rho_e - L_e} \right) \tag{15.}$$

The numerators r_e and s_e are

$$\text{if } \frac{\partial c}{\partial \rho_e}(\rho^0) > 0 \text{ then } r_e = (U_e - \rho_e^0)^2 \frac{\partial c}{\partial \rho_e}(\rho^0) \text{ and } s_e = 0 \tag{16.}$$

and

$$\text{if } \frac{\partial c}{\partial \rho_e}(\rho^0) < 0 \text{ then } s_e = (\rho_e^0 - L_e)^2 \frac{\partial c}{\partial \rho_e}(\rho^0) \text{ and } r_e = 0 \qquad (17.)$$

Since the sensitivity of the objective function is found to be negative for all elements $e = 1, \ldots, N$, the objective function becomes an explicit function:

$$c(\rho) \approx c(\rho^0) - \sum_{e=1}^{N} \left(\frac{(\rho_e^0 - L_e)^2}{\rho_e - L_e} \frac{\partial c}{\partial \rho_e}(\rho^0) \right) \qquad (18.)$$

The objective function minimization subproblem at each iteration K becomes

$$\min_{\rho_e} \left[c(\rho^0) - \sum_{e=1}^{N} \left(\frac{(\rho_e^0 - L_e)^2}{\rho_e - L_e} \frac{\partial c}{\partial \rho_e}(\rho^0) \right) \right]$$

$$\text{s.t. } \sum_{e=1}^{N} v_e \rho_e \leq V \qquad (19.)$$

$$0 \leq \rho_{min} \leq \rho_e \leq 1, \qquad e = 1, \ldots, N$$

The minimization of the objective function uses the Lagrangian functional and a dual method. The Lagrangian functional

$$L = c(\rho^0) - \sum_{e=1}^{N} \left(\frac{(\rho_e^0 - L_e)^2}{\rho_e - L_e} \frac{\partial c}{\partial \rho_e}(\rho^0) \right) + \Lambda \left[\sum_{e=1}^{N} v_e \rho_e - V \right] \qquad (20.)$$

Is to be minimized with respect to density. This is a separable and convex functional, so it is an allegedly straightforward calculation. This functional is then maximized with respect to Λ. This acts to adjust the value of Λ so that the volume constraint is satisfied. TWhile

TOSCA has modified the MMA-SIMP algorithm, an idea of how to update element densities is now shown.

If L_e is 0, the element's new density is calculated by

$$\rho_{K+1_e} = \begin{cases} \rho_{\min} & \text{if } \rho_K B_K^\eta \leq \rho_{\min} \\ 1 & \text{if } \rho_K B_K^\eta \geq 1 \\ \rho_K B_K^\eta & \text{otherwise} \end{cases} \tag{21.}$$

Where B_K is the ratio of strain energy densities between step iterations, the move limit, ξ, is ∞, and the tuning parameter, η, $= 0.5$. The strain energy density ratio B_K is given by

$$B_{K_e} = \frac{p\rho_e^{p-1} E_{ijkl}^0 \varepsilon_{ij}(u_K)\varepsilon_{kl}(u_K)}{\Lambda_K} \tag{22.}$$

Where Λ_K is the Lagrange multiplier maximized in the dual maximization. When $B_K = 1$, a local optimum is reached; when $B_K < 1$ the algorithm adds material to the element (increases its density) and when $B_K > 1$ the algorithm removes material from the element. From above, the Λ_K term is a Lagrange multiplier, and is the strain energy density value that satisfies the volume constraint.

APPENDIX B. ADDITIONAL RESULTS FROM FEA

This section provides more images of the finite element modeling results of the stock, printable, and optimized geometries.

B.1 FE Results of Stock Geometry

B.1.1 In-Plane Hydraulic Loading

Figure 46 shows the effect of in-plane loading on the flanges. All of the material immediately surrounding the lugs see much higher loading than the box structure in the center.
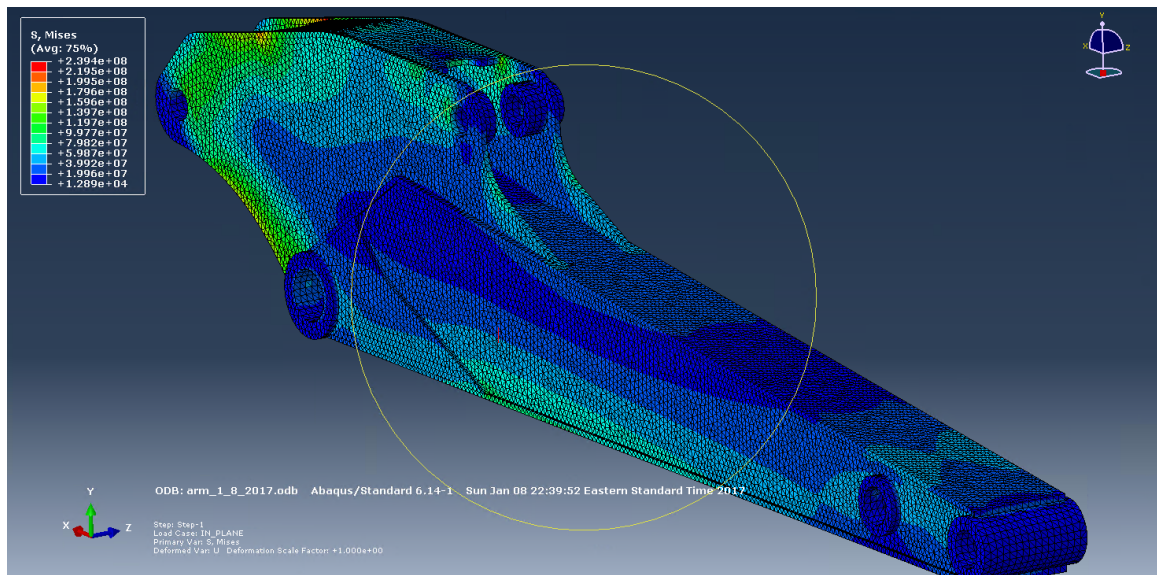
Figure 46. Additional views of in-plane loading

Figure 47 shows a close up of the stress due to in-plane hydraulic cylinder loading for the stock geometry. The load transfer from the welded lug to the flanges can be clearly seen in the figure.
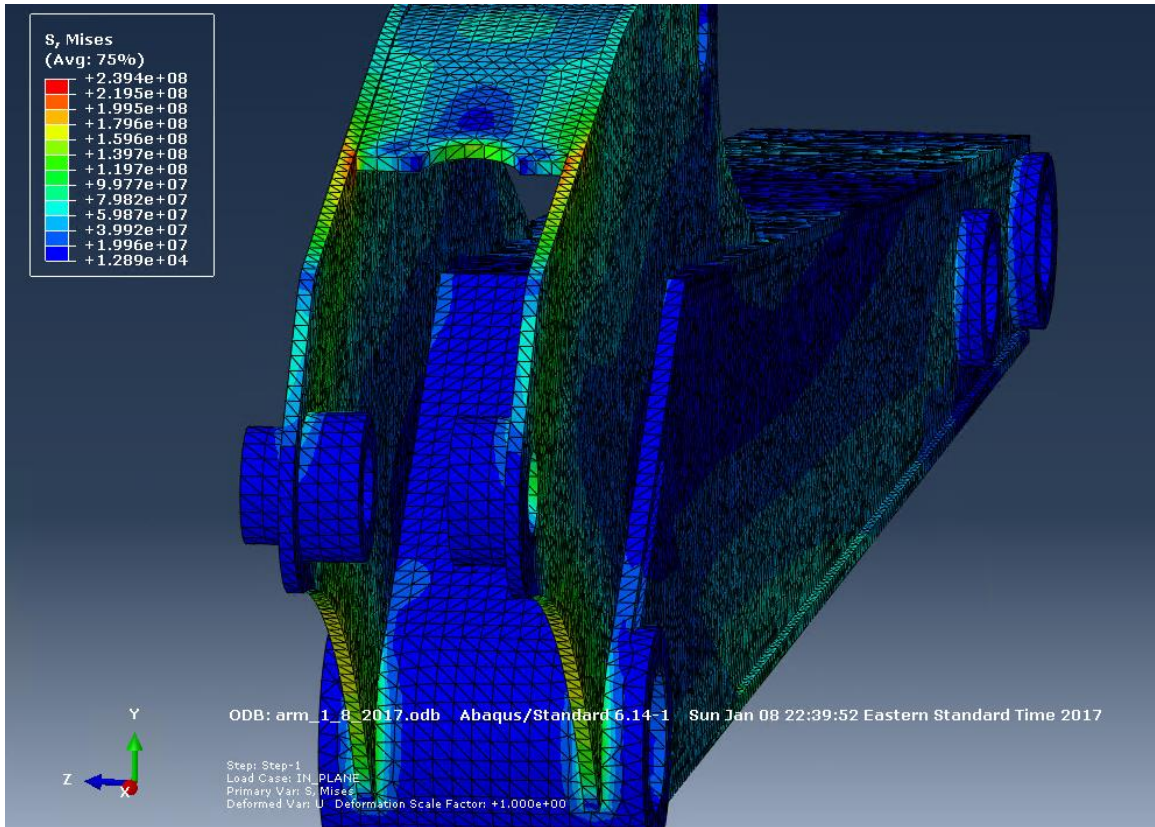
Figure 47. Close-up of end of arm under in-plane loads.

B.1.2 Side Loading

The alternative side view in Figure 48 further illustrates the setup of a neutral axis in bending. The location where the flange attaches to the box structure has a stress concentration of around 200 MPa. The stock arm has a weld build-up at this spot to ease the concentration; a similar build-up on the lug that attaches the bucket cylinder to the arm also has a weld build-up to ease the stress.

Figure 48. Side view of side loads in stock geometry.

The rear portion of the stock arm does not experience high stresses during side and torsion load. The load is transferred to the section between the point of application, which is the lug connecting the bucket to the arm, and the lug pinning the arm to the boom. The flanges thus do not experience a high stress state, as shown in Figure 49.
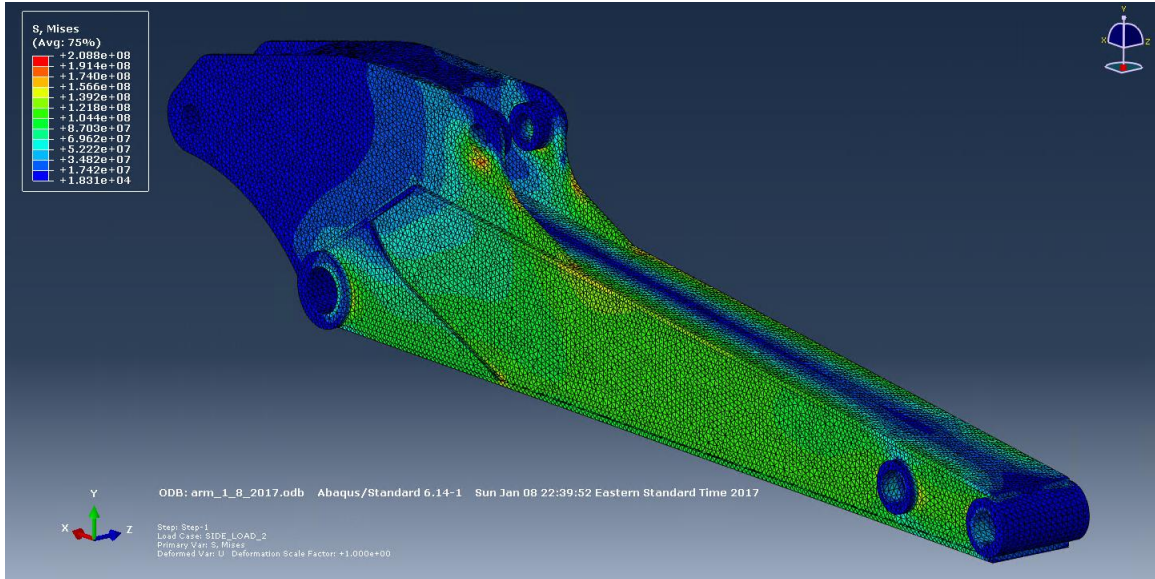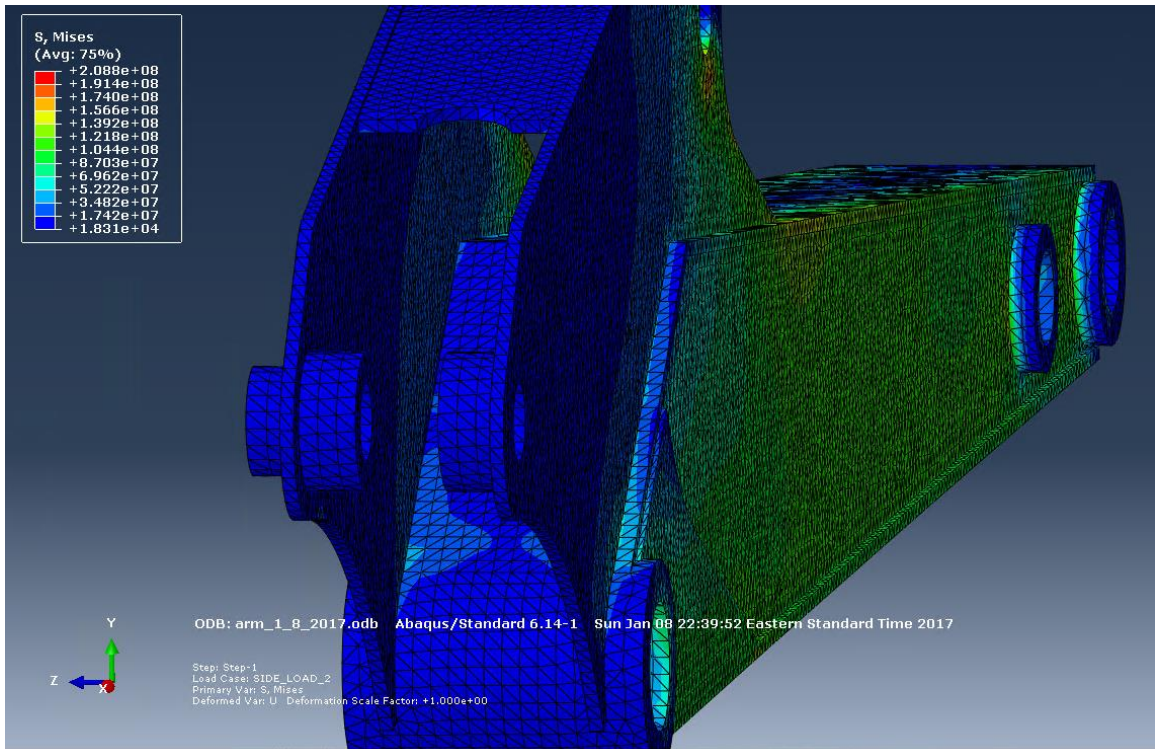
Figure 49. Rear view of arm under side loading.

B.2 FE Results of Printable Geometry

This section shows the FE analysis on the printable geometry. The printable geometry is the starting point for the topology optimization.

B.2.1 In-Plane Hydraulic Cylinder Loading

The stress state from the in-plane hydraulic cylinder loads on the printable geometry are shown in Figure 50. The stresses are lower than the stock geometry, but this design is heavier due to the integrated hydraulic lines. The flanges, which are approximately the same geometry as the stock design, undergo the majority of the stress. The lug connecting to the arm cylinder has a high stress concentration. As noted in the stock design results, the

stress concentration is lowered using a weld build-up, which will be taken into account in the final geometry.
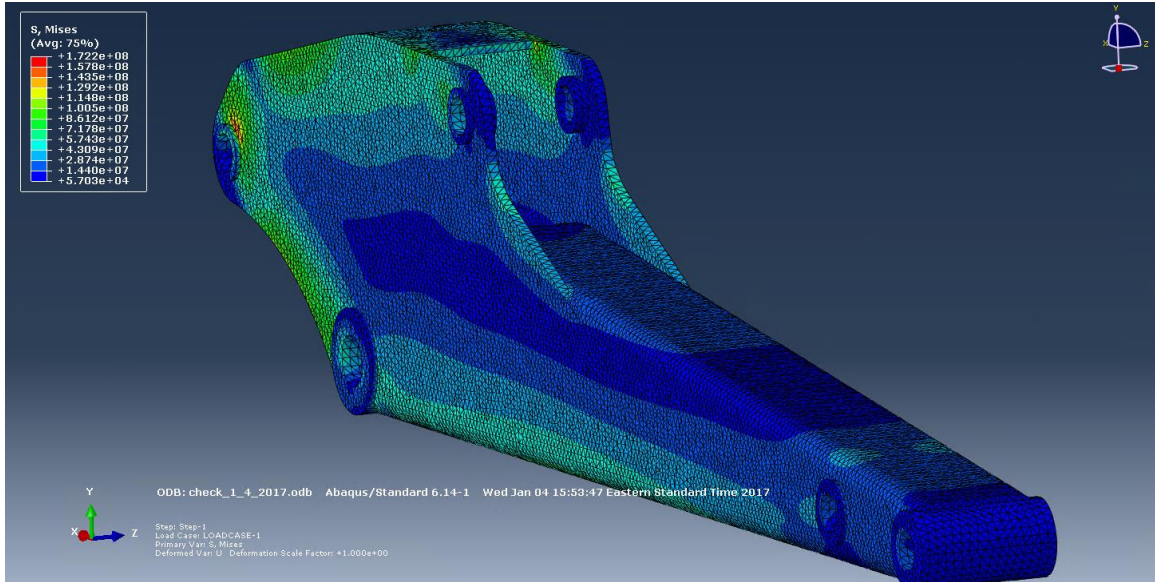
Figure 50. Side view of hydraulic cylinder loading on printable geometry.

A close up view of the printable geometry under in-plane loading is shown in Figure 51. A stress concentration is seen where the flange support joins the flange; the maximum stress there is approximately 170 MPa. The location of the flange support joining features lower stress values than expected due to the sharp joint, but the same location is highly stressed under the side and torsion load.
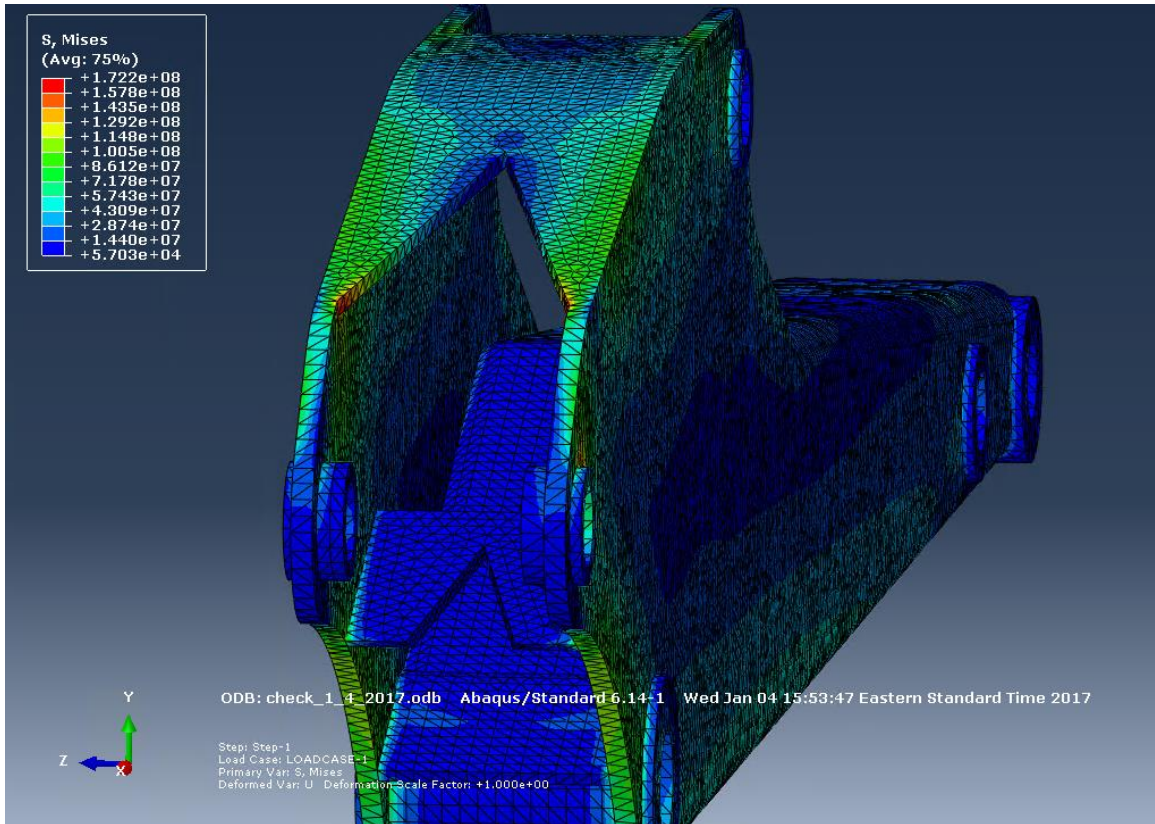
Figure 51. Rear view of printable geometry with hydraulic loading.

A cutaway view of the in-plane loads on the printable geometry is shown in Figure 52. The bottom of the arm sees a high stress, while the top does not. This is due to the integrated hydraulic lines providing extra stiffness.
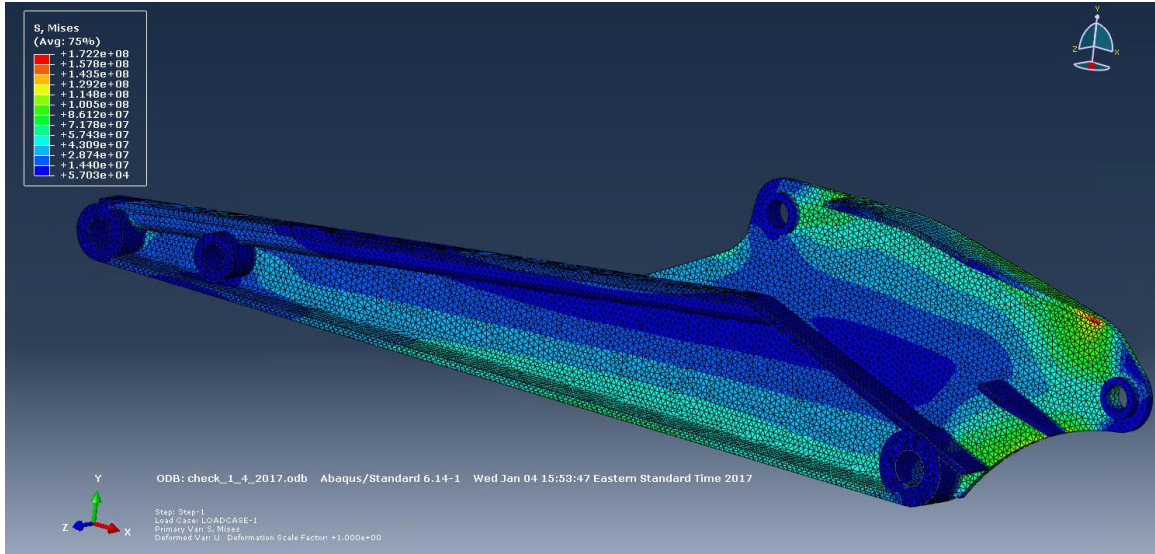
Figure 52. Cutaway view of the hydraulic cylinder loads on the printable geometry.

B.2.2 Side Loading

The side loading results on the printable geometry are shown in Figure 53. The printable geometry does not have a reinforcing plate at the lug pinning the arm to the boom, so a stress concentration is present. Even without the reinforcement plate, the stress state of 206 MPa is within the limit of the allowable design stress.
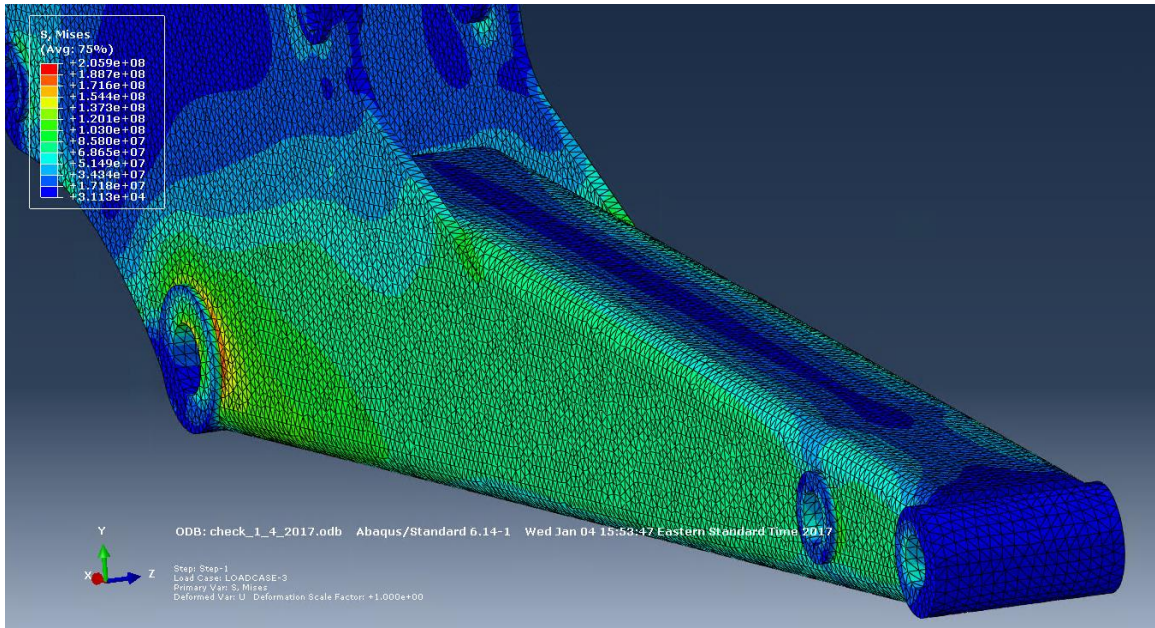
Figure 53. Side view of side loading on printable geometry.

A view of the flange support is shown in Figure 54. The location where the support meets causes a stress concentration; the stress is less than 200 MPa so it is not a limiting factor in determining the life of the arm. The stress concentration could be reduced by filling in the "V" groove via manual weld deposition after the part is built, but that adds to the complexity of post processing.
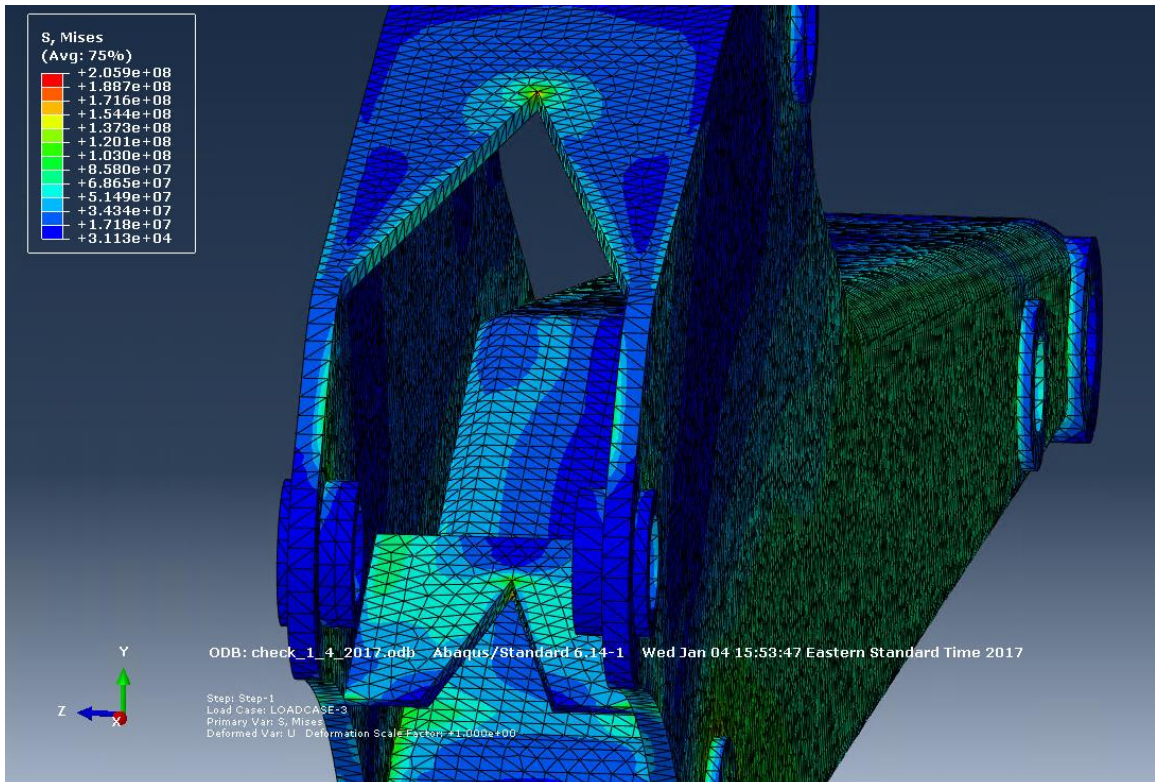
Figure 54. Side loading on printable geometry.

These results show why the topology optimization algorithm removed much of the top of the box section. The integrated hydraulic lines provided extra stiffness such that the need for the top of the box section was not needed. The final arm geometry does not have the hydraulic lines in the same location, but the finite element analysis shows that the arm does not surpass the allowable design stress.

B.4 FE Results of Final Arm Geometry

Extra results from the re-interpreted geometry are shown in this section. The stress results compare well to the previous arm designs.

B.4.1 In-Plane Hydraulic Cylinder Loading

The highly stressed region for the hydraulic cylinder loading is on the flanges, as in the original, printable, and optimized geometry. The distribution is shown in Figure 55. The box section has increased stiffness from the hydraulic lines and thicker walls by the pin joint that attaches the arm to the boom.
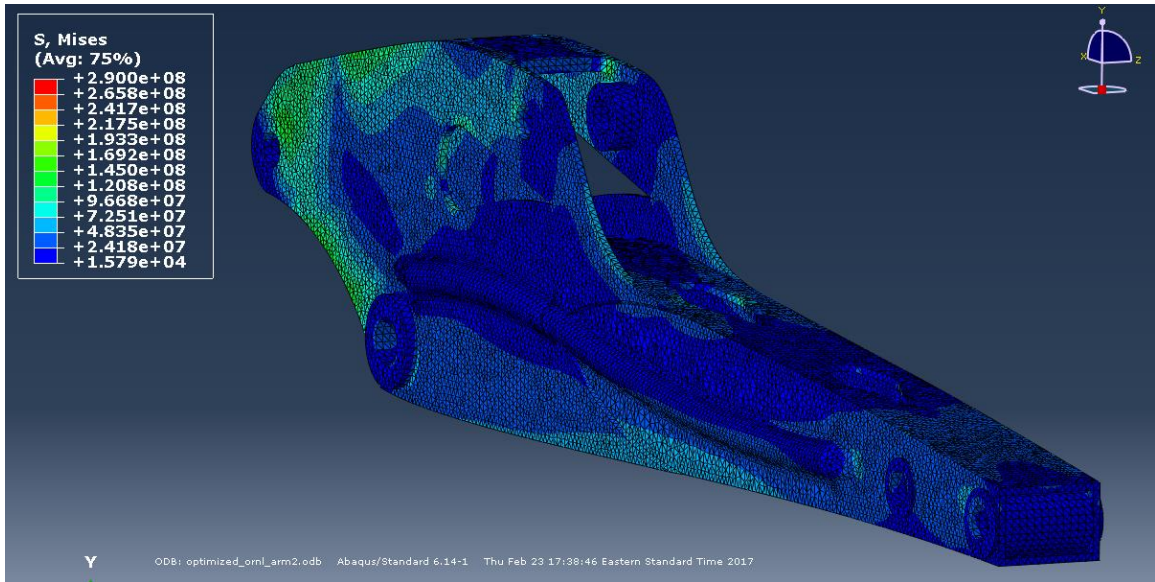
Figure 55. Stress distribution for cylinder loads on the ORNL re-interpreted arm.

The stress concentration where the flange supports start are shown in Figure 56. This view shows the stress concentration where the flange supports meet with the flange. The reentrant design of the flange support results in a stress singularity under the compressive digging loads.
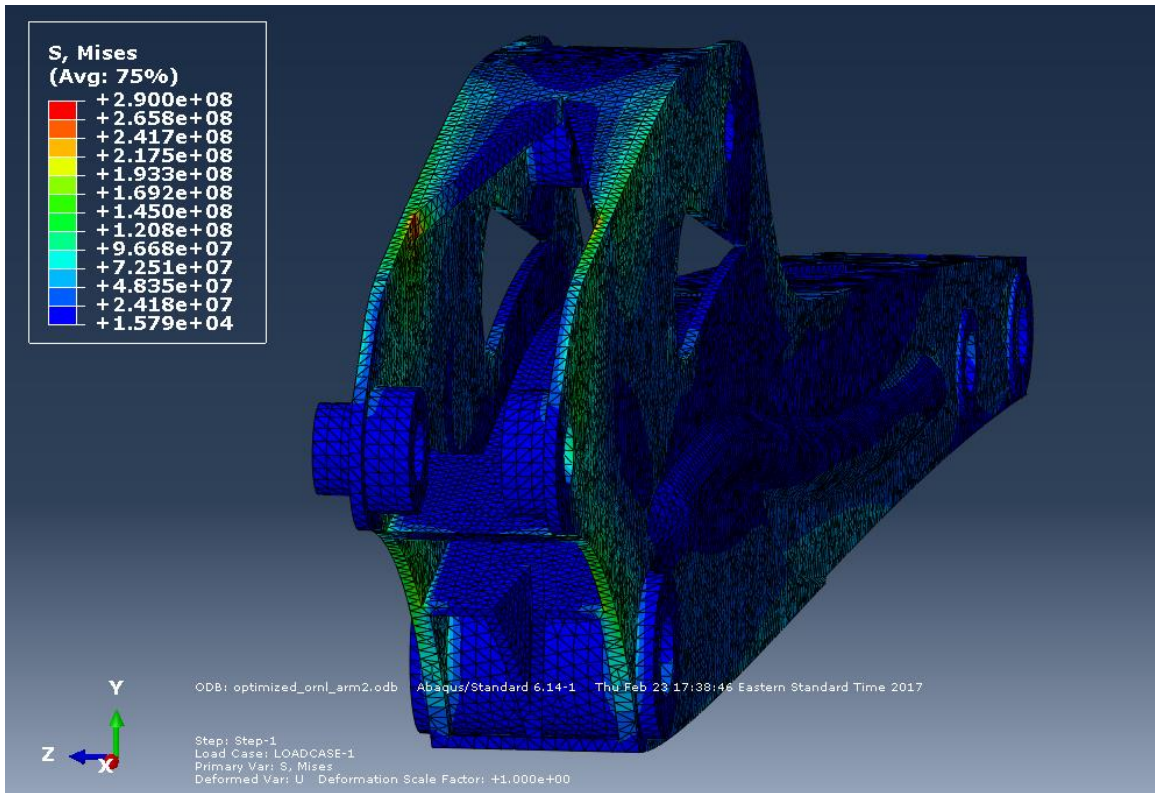
Figure 56. Rear view of ORNL arm.

The cutaway view of the final arm geometry is shown in Figure 57. The stresses are low through the box section and the middle of the flanges. The holes see the usual stress concentrations, but the stresses are within the limits of the allowable design stress.
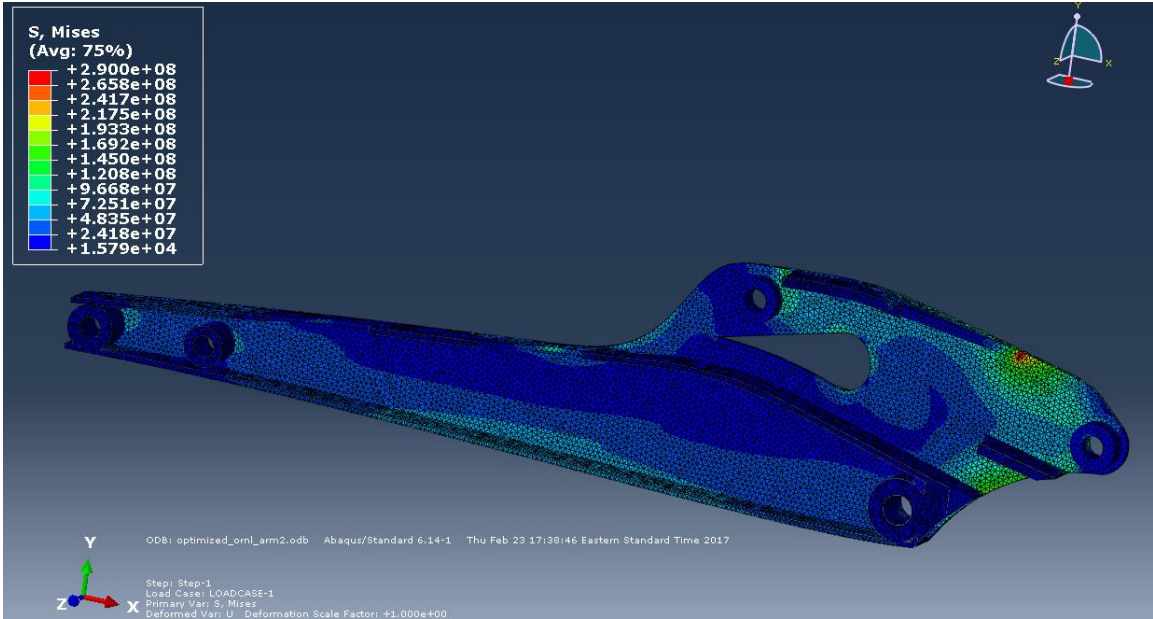
Figure 57. Cutaway of ORNL arm undergoing in-plane hydraulic cylinder loading.

B.4.2 Side and Torsion Loading

The side and torsion load case need only result in the arm not being damaged under load. Thus, maintaining the maximum stress under the conservative design stress of 250 MPa is all that is needed. An angled view of the stress state in the arm due to the side and torsion loading is shown in Figure 58. The maximum stress is located where the hydraulic lines begin protruding from the box structure. It appears that this stress is a singularity as well, as mesh convergence tests have shown. The stress concentration is not expected to impact the performance of the printed and installed excavator arm.
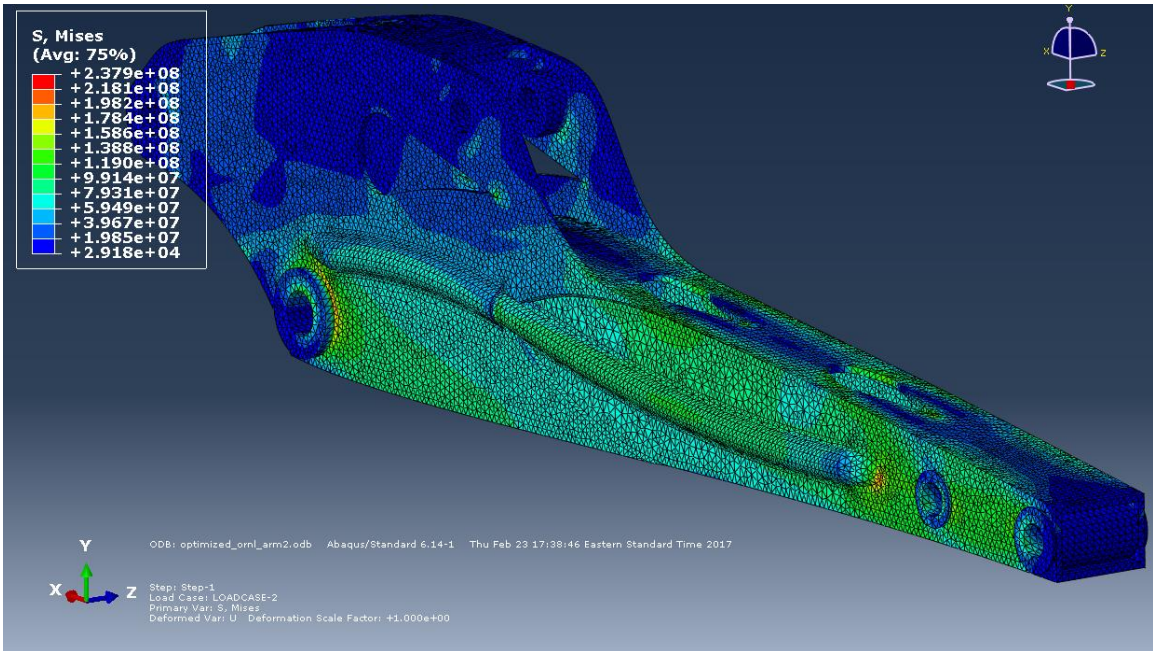
Figure 58. Side and torsion loading stress distribution on ORNL arm.

A rear view of the final arm geometry undergoing side and torsion loading is shown in Figure 59. The figure clearly shows that the flanges are not highly stressed when undergoing the side and torsion loading, since the load path is from the point of application, which is the lug that pins to the bucket, and the pin joint between the boom and the arm. The location where the flange support bridges shows a slight concentration, but not significant enough to impact the excavator performance.
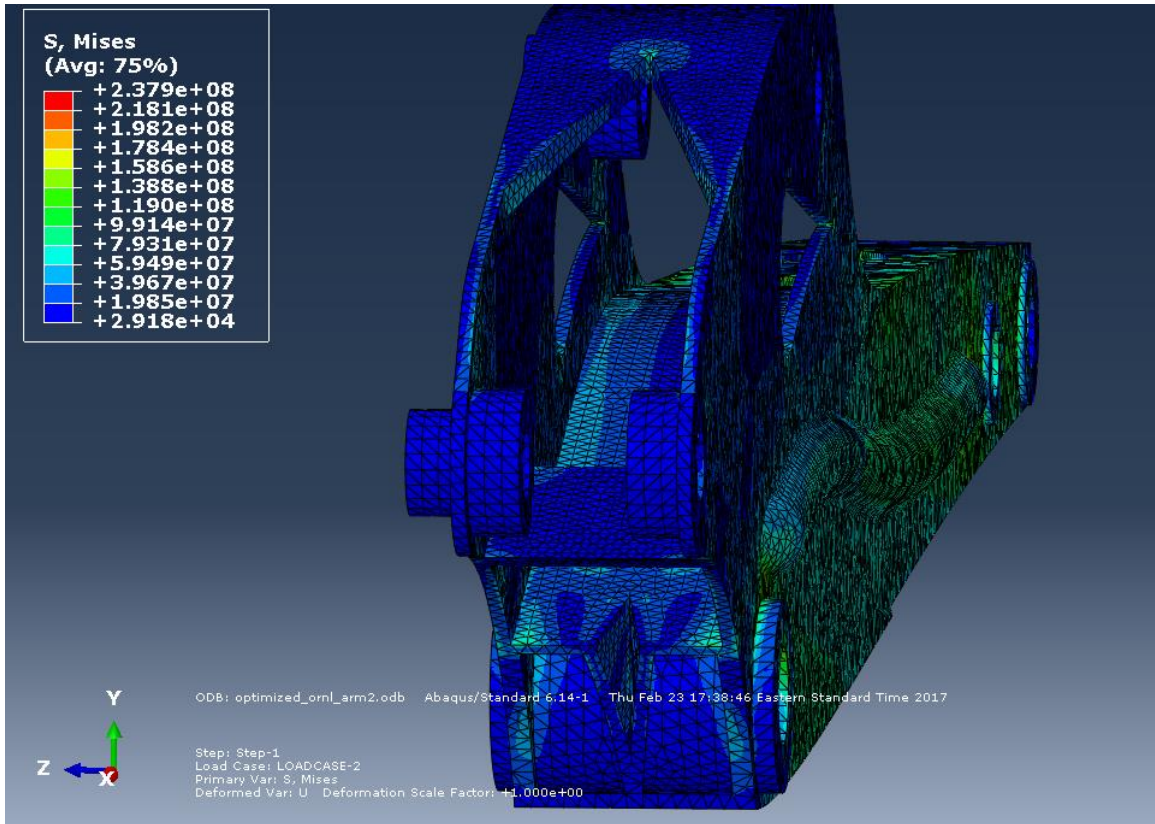
Figure 59. Rear view of side and torion loading on ORNL arm geometry.

The side and torsion loading have a neutral axis, as expected from the previous results, shown in Figure 60. The holes in the top of the box section are thus well placed, since the top is not highly stressed in both the side and torsion and the in-plane hydraulic cylinder loads.
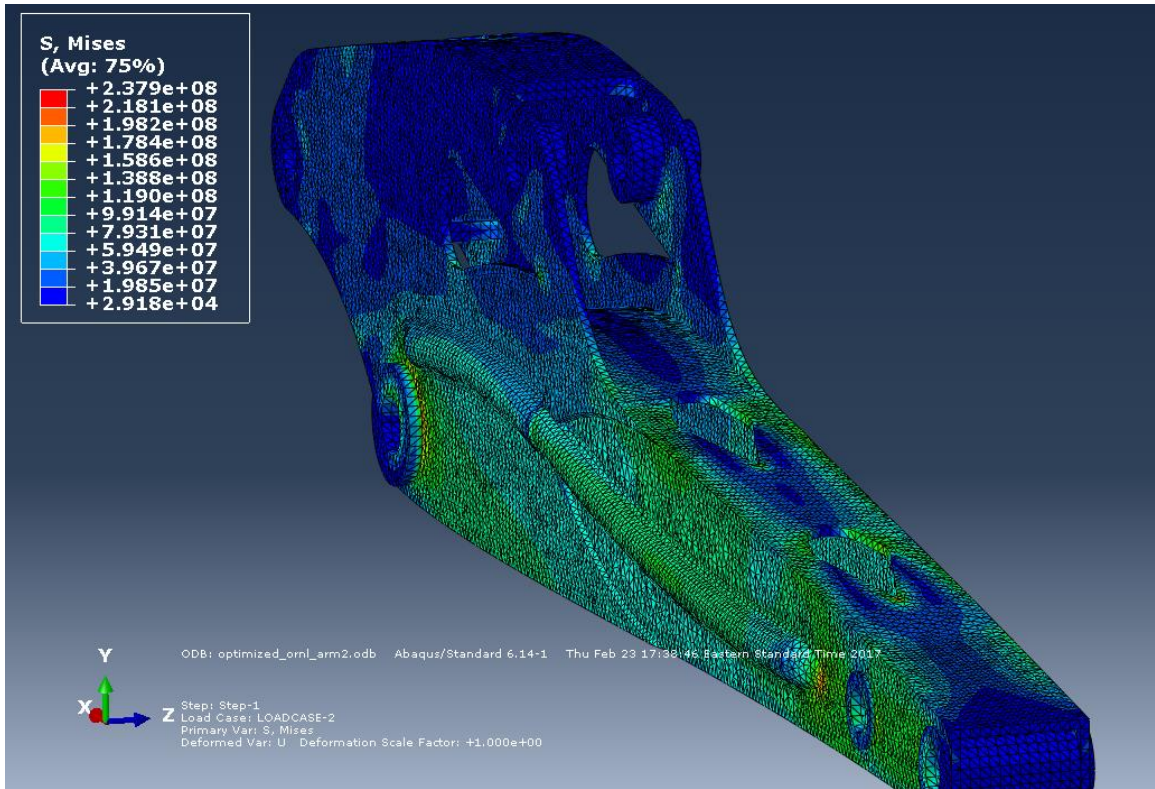
Figure 60. Alternate view of side and torsion loading stress distribution on ORNL arm geometry.

REFERENCES

[1]   "3D Printing," *Tufts Maker Network*. [Online]. Available: https://maker.tufts.edu/handbooks/3d-printing. [Accessed: 12-Mar-2017].

[2]   C. W. Hull, "Apparatus for production of three-dimensional objects by stereolithography," 11-Mar-1986.

[3]   X. Yan and P. Gu, "A review of rapid prototyping technologies and systems," *Comput. Des.*, vol. 28, no. 4, pp. 307–318, Apr. 1996.

[4]   "Stereolithography | Stratasys Direct Manufacturing." [Online]. Available: https://www.stratasysdirect.com/solutions/stereolithography/. [Accessed: 12-Mar-2017].

[5]   K. Chockalingam, N. Jawahar, and U. Chandrasekhar, "Influence of layer thickness on mechanical properties in stereolithography," *Rapid Prototyp. J.*, vol. 12, no. 2, pp. 106–113, Mar. 2006.

[6]   G. V. Salmoria, F. H. Lafratta, M. M. Biava, C. H. Ahrens, and P. Z. Ferreira, "Rapid manufacturing and rapid tooling of polymer miniaturized parts using Stereolithography," *J. Brazilian Soc. Mech. Sci. Eng.*, vol. 30, no. 1, pp. 7–10, Mar. 2008.

[7]   "Formlabs." [Online]. Available: https://formlabs.com/support/faq/. [Accessed: 13-Mar-2017].

[8]   B. N. Turner and S. A. Gold, "A review of melt extrusion additive manufacturing processes: II. Materials, dimensional accuracy, and surface roughness," *Rapid*

Prototyp. J., vol. 21, no. 3, pp. 250–261, Apr. 2015.

[9]   A. Bournias-Varotsis, "Industrial FDM vs. Desktop FDM | 3D Hubs," *3D Hubs*. [Online]. Available: https://www.3dhubs.com/knowledge-base/industrial-fdm-vs-desktop-fdm#accuracy. [Accessed: 12-Mar-2017].

[10]   D. K. Ahn, J. H. Kweon, J. H. Choi, and S. H. Lee, "Relation between Surface Roughness and Overlap Interval in Fused Deposition Modeling," *Adv. Mater. Res.*, vol. 264–265, pp. 1625–1630, Jun. 2011.

[11]   I. Zein, D. W. Hutmacher, K. C. Tan, and S. H. Teoh, "Fused deposition modeling of novel scaffold architectures for tissue engineering applications," *Biomaterials*, vol. 23, no. 4, pp. 1169–1185, 2002.

[12]   S.-H. Ahn, M. Montero, D. Odell, S. Roundy, and P. K. Wright, "Anisotropic material properties of fused deposition modeling ABS," *Rapid Prototyp. J.*, vol. 8, no. 4, pp. 248–257, 2002.

[13]   C. E. Duty *et al.*, "Structure and mechanical behavior of Big Area Additive Manufacturing (BAAM) materials Structure and Mechanical Behavior of Big Area Additive Manufacturing (BAAM) Materials," *Rapid Prototyp. J.*, vol. 23, no. 1, 2017.

[14]   "Solidoodle." [Online]. Available: http://cdn2.vox-cdn.com/assets/4860274/Solidoodle_New_Products_Spec_Sheet.pdf. [Accessed: 13-Mar-2017].

[15]   "Fortus 900mc," *Stratasys*. [Online]. Available: http://usglobalimages.stratasys.com/Main/Files/Machine_Spec_Sheets/PSS_FDM_

Fortus900mc.pdf?v=636125663318893675#_ga=1.32875450.522642979.1489417

668. [Accessed: 13-Mar-2017].

[16] F. Ning, W. Cong, J. Wei, S. Wang, and M. Zhang, "Additive Manufacturing of
Cfrp Composites Using Fused Deposition Modeling: Effects of Carbon Fiber
Content and Length," vol. 1989, pp. 1–7, 2015.

[17] S. Robarts, "'World's first' 3D printed car created and driven by Local Motors,"
New Atlas, 2014. [Online]. Available: http://newatlas.com/local-motors-strati-
imts/33846/. [Accessed: 16-Feb-2017].

[18] K. Biswas *et al.*, "Additive Manufacturing Integrated Energy—Enabling Innovative
Solutions for Buildings of the Future," *J. Sol. Energy Eng.*, vol. 139, no. 1, p. 15001,
Nov. 2016.

[19] C. Westbook, "How to design 3D printed pin hinges: No assembly required –
Ponoko Help Center," 2016. [Online]. Available: http://support.ponoko.com/hc/en-
us/articles/220290728-How-to-design-3D-printed-pin-hinges-No-assembly-
required. [Accessed: 26-Mar-2017].

[20] S. Cahoon, "MatterHackers Lab: Design 3D Printed Assemblies," 2016. [Online].
Available: https://www.matterhackers.com/articles/matterhackers-lab:-design-
assemblies-. [Accessed: 26-Mar-2017].

[21] D. M. Keicher *et al.*, "Laser Engineered Net Shaping (LENS {trademark}) for
additive component processing," in *CONF-9604141--1*, 1996.

[22] M. L. Griffith *et al.*, "FREE FORM FABRICATION OF METALLIC
COMPONENTS USING LASER ENGINEERED NET SHAPING (LENS^{TM})," in

Solid Freeform Fabrication, 1996.

[23]   D. (Ed) Benjamin and C. W. (Ed) Kirkpatrick, "Handbook, Properties and selection: stainless steels, tool materials and special-purpose metals," *Metals, ASM*. ASM Int Met, pp. 113–121, 1980.

[24]   A. Yadollahi, N. Shamsaei, S. M. Thompson, and D. W. Seely, "Effects of process time interval and heat treatment on the mechanical and microstructural properties of direct laser deposited 316L stainless steel," *Mater. Sci. Eng. A*, vol. 644, pp. 171–183, 2015.

[25]   G. K. Lewis and E. Schlienger, "Practical considerations and capabilities for laser assisted direct metal deposition," *Mater. Des.*, vol. 21, no. 4, pp. 417–423, 2000.

[26]   D. Keicher *et al.*, "Free form fabrication using the laser engineered net shaping (LENS {trademark}) process," Albuquerque, NM, 1996.

[27]   "Direct Metal Deposition Fabrication Process for Metal 3D Prints." [Online]. Available: https://www.sculpteo.com/en/glossary/dmd-definition/. [Accessed: 12-Mar-2017].

[28]   "LENS Metal Additive Manufacturing Product Family," *Optomec*, 2016. [Online]. Available: http://www.multistation.com/IMG/pdf/brochure_optomec_novembre_2016.pdf. [Accessed: 03-Apr-2017].

[29]   "Large metal component part repair - LENS 850-R Systems." [Online]. Available: https://www.optomec.com/3d-printed-metals/lens-printers/metal-component-repair-3d-printer/. [Accessed: 03-Apr-2017].

[30] M. L. Griffith *et al.*, "Understanding the Microstructure and Properties of Components Fabricated by Laser Engineered Net Shaping (LENS)," in *MRS Proceedings*, 2000, vol. 625, p. 9.

[31] P. Mercelis and J.-P. Kruth, "Residual stresses in selective laser sintering and selective laser melting," *Rapid Prototyp. J.*, vol. 12, no. 5, pp. 254–265, 2006.

[32] J.-P. Kruth, P. Mercelis, J. Vaerenbergh, L. Froyen, and M. Rombouts, "Binding mechanisms in selective laser sintering and selective laser melting," *Rapid Prototyp. J.*, vol. 11, no. 1, pp. 26–36, 2005.

[33] B. Vrancken, L. Thijs, J.-P. Kruth, and J. Van Humbeeck, "Heat treatment of Ti6Al4V produced by Selective Laser Melting: Microstructure and mechanical properties," *J. Alloys Compd.*, vol. 541, pp. 177–185, 2012.

[34] G. Strano, L. Hao, R. M. Everson, and K. E. Evans, "Surface roughness analysis, modelling and prediction in selective laser melting," *J. Mater. Process. Technol.*, vol. 213, no. 4, pp. 589–597, 2013.

[35] "X LINE 2000R Technical Data," *Concept Laser*. [Online]. Available: http://www.conceptlaserinc.com/wp-content/uploads/2016/11/1016_X-line-2000R_US_highres.compressed.pdf. [Accessed: 13-Mar-2017].

[36] F. Abe, K. Osakada, M. Shiomi, K. Uematsu, and M. Matsumoto, "The manufacturing of hard tools from metallic powders by selective laser melting," *J. Mater. Process. Technol.*, vol. 111, no. 1–3, pp. 210–213, 2001.

[37] B. Vayre, F. Vignat, and F. Villeneuve, "Identification on Some Design Key Parameters for Additive Manufacturing: Application on Electron Beam Melting,"

Procedia CIRP, vol. 7, pp. 264–269, 2013.

[38] J. J. Lewandowski and M. Seifi, "Metal Additive Manufacturing: A Review of Mechanical Properties," *Annu. Rev. Mater. Res.*, vol. 46, no. 1, pp. 151–186, Jul. 2016.

[39] J. Hiemenz, "Electron Beam Melting," *Adv. Mater. Process.*, vol. 165, no. 3, pp. 45–46, 2007.

[40] "Arcam A2." .

[41] N. Kapustka and I. Harris, "Exploring Arc Welding for Additive Manufacturing of Titanium Parts," *Weld. J.*, vol. 93, no. 3, pp. 32–35, 2014.

[42] Z. Jandric, M. Labudovic, and R. Kovacevic, "Effect of heat sink on microstructure of three-dimensional parts built by welding-based deposition," *Int. J. Mach. Tools Manuf.*, vol. 44, no. 7, pp. 785–796, 2004.

[43] E. Brandl, A. Schoberth, and C. Leyens, "Morphology, microstructure, and hardness of titanium (Ti-6Al-4V) blocks deposited by wire-feed additive layer manufacturing (ALM)," *Mater. Sci. Eng. A*, vol. 532, pp. 295–307, 2012.

[44] J. Gockel, J. Beuth, and K. Taminger, "Integrated control of solidification microstructure and melt pool dimensions in electron beam wire feed additive manufacturing of Ti-6Al-4V," *Addit. Manuf.*, vol. 1, pp. 119–126, 2014.

[45] F. Martina, J. Mehnen, S. W. Williams, P. Colegrove, and F. Wang, "Investigation of the benefits of plasma deposition for the additive layer manufacture of Ti–6Al–4V," *J. Mater. Process. Technol.*, vol. 212, no. 6, pp. 1377–1386, 2012.

[46] T. Abe and H. Sasahara, "Dissimilar metal deposition with a stainless steel and

nickel-based alloy using wire and arc-based additive manufacturing," *Precis. Eng.*, vol. 45, pp. 387–395, 2016.

[47] C. Conrardy, "ASM Handbook Vol 6A Welding Fundamentals and Processes." pp. 309–317, 2011.

[48] E. Gharibshahiyan, A. H. Raouf, N. Parvin, and M. Rahimian, "The effect of microstructure on hardness and toughness of low carbon welded steel using inert gas welding," *Mater. Des.*, vol. 32, no. 4, pp. 2042–2048, 2011.

[49] M. Eroğlu, M. Aksoy, and N. Orhan, "Effect of coarse initial grain size on microstructure and mechanical properties of weld metal and HAZ of a low carbon steel," *Mater. Sci. Eng. A*, vol. 269, no. 1, pp. 59–66, 1999.

[50] T. Debroy and S. A. David, "Physical processes in fusion welding," *Rev. Mod. Phys.*, vol. 67, no. 1, pp. 85–112, 1995.

[51] Y. Shi and Z. Han, "Effect of weld thermal cycle on microstructure and fracture toughness of simulated heat-affected zone for a 800MPa grade high strength low alloy steel," *J. Mater. Process. Technol.*, vol. 207, no. 1, pp. 30–39, 2008.

[52] Y. Zhang, Y. Chen, P. Li, and A. T. Male, "Weld deposition-based rapid prototyping: a preliminary study," *J. Mater. Process. Technol.*, vol. 135, no. 2, pp. 347–357, 2003.

[53] J. J. Dike, J. A. Brooks, D. J. Bammann, M. Li, J. S. Krafcik, and N. Y. C. Yang, "SANDIA REPORT Predicting Weld Solidification Cracking Using Damage Mechanics -LDRD Summary Report," 1997.

[54] J. C. Lippold, "Solidification Behavior and Cracking Susceptibility of Pulsed-Laser

Welds in Austenitic Stainless Steels A shift in solidification behavior under rapid solidification conditions promotes an increase in cracking susceptibility," *Weld. J. Incl. Weld. Res. Suppl.*, vol. 73, no. 6, p. 129, 1994.

[55] V. Shankar, T. P. S. Gill, S. L. Mannan, and S. Sundaresan, "Solidification cracking in austenitic stainless steel welds," *Sadhana*, vol. 28, no. 3–4, pp. 359–382, Jun. 2003.

[56] T. C. Nguyen, D. C. Weckman, D. A. Johnson, and H. W. Kerr, "High speed fusion weld bead defects," *Sci. Technol. Weld. Join.*, vol. 11, no. 6, pp. 618–633, Nov. 2006.

[57] P. S. Wei, "Thermal Science of Weld Bead Defects: A Review," *J. Heat Transfer*, vol. 133, no. 3, p. 31005, 2011.

[58] H. W. Choi, D. F. Farson, and M. H. Cho, "Using a Hybrid Laser Plus GMAW Process for Controlling the Bead Humping Defect The heat input from a defocused laser beam applied in front of a GMAW pool suppresses formation of weld bead hump defects and allows higher travel speeds," *Weld. J.*, 2006.

[59] P. Withers, "Residual Stress and its Role in Failure," *Reports Prog. Phys.*, vol. 70, no. 12, 2007.

[60] S.-H. Park and D.-H. Lee, "Sequencing algorithms for multiple arc-welding robots considering thermal distortion," *Int. J. Prod. Res.*, vol. 46, no. 17, pp. 4751–4767, Sep. 2008.

[61] R. Lostado-Lorza, R. Fernández-Martínez, B. J. Mac Donald, and A. Ghani-Olabi, "Design and Optimization of Welded Products Using Genetic Algorithms, Model

Trees and the Finite Element Method," Springer, Cham, 2014, pp. 279–288.

[62] W. E. Frazier, "Metal Additive Manufacturing: A Review," *J. Mater. Eng. Perform.*, vol. 23, no. 6, pp. 1917–1928, Jun. 2014.

[63] G. Venturini, F. Montevecchi, A. Scippa, and G. Campatelli, "Optimization of WAAM Deposition Patterns for T-crossing Features," *Procedia CIRP*, vol. 55, pp. 95–100, 2016.

[64] K. Svanberg, "The method of moving asymptotes—a new method for structural optimization," *Int. J. Numer. Methods Eng.*, vol. 24, no. 2, pp. 359–373, Feb. 1987.

[65] J. K. Guest and M. Zhu, "Casting and Milling Restrictions in Topology Optimization via Projection-Based Algorithms," in *Volume 3: 38th Design Automation Conference, Parts A and B*, 2012, p. 913.

[66] J. K. Guest, "Topology optimization with multiple phase projection," *Comput. Methods Appl. Mech. Eng.*, vol. 199, no. 1, pp. 123–135, 2009.

[67] Y. Y. Xiu and S. Liang, "Topology optimization and digital manufacturing of stress-constrained structure based on level set method," *Appl. Mech. Mater.*, vol. 556–562, pp. 4202–4205, 2014.

[68] N. P. Van Dijk, K. Maute, M. Langelaar, and F. Van Keulen, "Level-set methods for structural topology optimization: A review," *Struct. Multidiscip. Optim.*, vol. 48, no. 3, pp. 437–472, 2013.

[69] J. Liu and Y.-S. Ma, "3D level-set topology optimization: a machining feature-based approach," *Struct. Multidiscip. Optim.*, vol. 52, no. 3, pp. 563–582, Sep. 2015.

[70] M. Burger and R. Stainko, "Phase-Field Relaxation of Topology Optimization with

Local Stress Constraints," *SIAM J. Control Optim.*, vol. 45, no. 4, pp. 1447–1466, Jan. 2006.

[71] X. Huang and Y. M. Xie, "Convergent and mesh-independent solutions for the bi-directional evolutionary structural optimization method," *Finite Elem. Anal. Des.*, vol. 43, no. 14, pp. 1039–1049, 2007.

[72] G. I. N. Rozvany, M. Zhou, and T. Birker, "Generalized shape optimization without homogenization," *Struct. Optim.*, vol. 4, no. 3–4, pp. 250–252, Sep. 1992.

[73] M. Stolpe and K. Svanberg, "An alternative interpolation scheme for minimum compliance topology optimization," *Struct. Multidiscip. Optim.*, vol. 22, no. 2, pp. 116–124, Sep. 2001.

[74] O. Sigmund, "On the usefulness of non-gradient approaches in topology optimization," *Struct. Multidiscip. Optim.*, vol. 43, no. 5, pp. 589–596, May 2011.

[75] S. D. Rajan, "Sizing, Shape, and Topology Design Optimization of Trusses Using Genetic Algorithm," *J. Struct. Eng.*, vol. 121, no. 10, pp. 1480–1487, Oct. 1995.

[76] A. G. M. Michell, "LVIII. *The limits of economy of material in frame-structures*," *Philos. Mag. Ser. 6*, vol. 8, no. 47, pp. 589–597, Nov. 1904.

[77] C. S. Edwards, H. A. Kim, and C. J. Budd, "An evaluative study on ESO and SIMP for optimising a cantilever tie—beam," *Struct. Multidiscip. Optim.*, vol. 34, no. 5, pp. 403–414, Sep. 2007.

[78] O. Sigmund and J. Petersson, "Numerical instabilities in topology optimization: A survey on procedures dealing with checkerboards, mesh-dependencies and local minima," *Struct. Optim.*, vol. 16, no. 1, pp. 68–75, 1998.

[79] J. Liu and Y. Ma, "A survey of manufacturing oriented topology optimization methods," *Adv. Eng. Softw.*, vol. 100, pp. 161–175, 2016.

[80] O. Sigmund, "Manufacturing tolerant topology optimization," *Acta Mech. Sin. Xuebao*, vol. 25, no. 2, pp. 227–239, 2009.

[81] K. T. Zuo, L. P. Chen, Y. Q. Zhang, and J. Yang, "Manufacturing- and machining-based topology optimization," *Int. J. Adv. Manuf. Technol.*, vol. 27, no. 5–6, pp. 531–536, 2006.

[82] A. T. Gaynor and J. K. Guest, "Topology Optimization for Additive Manufacturing: Considering Maximum Overhang Constraint."

[83] D. Brackett, I. Ashcroft, and R. Hague, "Topology optimization for additive manufacturing," *Solid Free. Fabr. Symp.*, pp. 348–362, 2011.

[84] R. Rezaie, M. Badrossamay, A. Ghaie, and H. Moosavi, "Topology optimization for fused deposition modeling process," *Procedia CIRP*, vol. 6, pp. 521–526, 2013.

[85] M. Langelaar, "Topology optimization of 3D self-supporting structures for additive manufacturing," *Addit. Manuf.*, vol. 12, pp. 60–70, 2016.

[86] D. Brackett, I. Ashcroft, and R. Hague, "TOPOLOGY OPTIMIZATION FOR ADDITIVE MANUFACTURING."

[87] A. Aremu, I. Ashcroft, R. Hague, R. Wildman, and C. Tuck, "Suitability of SIMP and BESO topology optimization algorithms for additive manufacture," in *Twenty First Annual International Solid Freeform Fabrication Symposium*, 2010, pp. 679–692.

[88] T. Gao and W. Zhang, "A mass constraint formulation for structural topology

optimization with multiphase materials," *Int. J. Numer. Methods Eng.*, vol. 88, no. 8, pp. 774–796, Nov. 2011.

[89] "Lincoln Electric." [Online]. Available: http://www.lincolnelectric.com/en-us/Pages/default.aspx. [Accessed: 08-Apr-2017].

[90] "3ders.org - Multiple 3D printing processes bring Additive Manufactured Excavator (AME) to life | 3D Printer News & 3D Printing News," 2017. [Online]. Available: http://www.3ders.org/articles/20170308-multiple-3d-printing-processes-bring-additive-manufactured-excavator-ame-to-life.html. [Accessed: 31-Mar-2017].

[91] M. P. Bendsøe and O. Sigmund, *Topology Optimization: Theory, Methods, and Applications*. New York: Springer-Verlag, 2003.